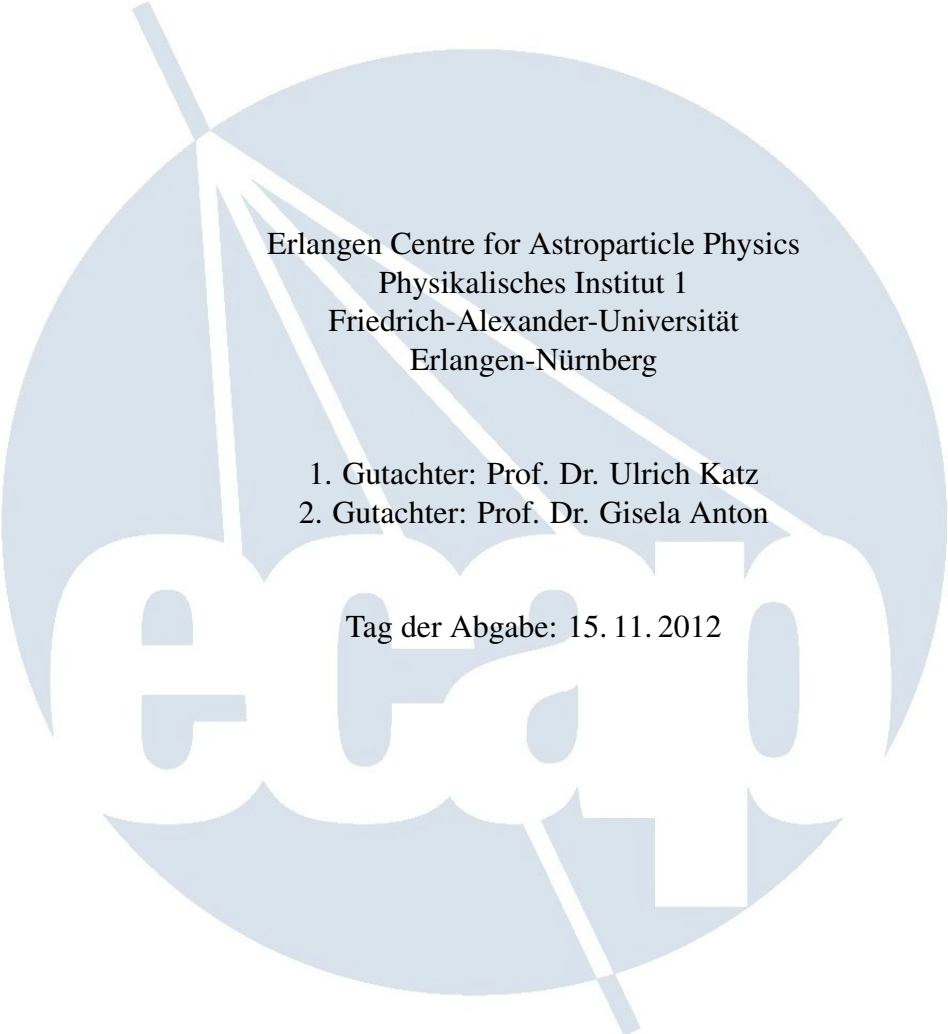


# **Characterisation of photomultiplier tube models to be used in the KM3NeT project**

Masterarbeit

vorgelegt von  
Jonas Reubelt



Erlangen Centre for Astroparticle Physics  
Physikalisches Institut 1  
Friedrich-Alexander-Universität  
Erlangen-Nürnberg

1. Gutachter: Prof. Dr. Ulrich Katz
2. Gutachter: Prof. Dr. Gisela Anton

Tag der Abgabe: 15. 11. 2012









# Contents

<b>1</b>	<b>Motivation</b>	<b>7</b>
<b>2</b>	<b>Cosmic rays</b>	<b>9</b>
<b>3</b>	<b>Neutrinos</b>	<b>13</b>
3.1	Neutrino production . . . . .	13
3.2	Neutrino interaction . . . . .	14
<b>4</b>	<b>Underwater neutrino telescopes</b>	<b>17</b>
4.1	Cherenkov radiation . . . . .	17
4.2	ANTARES . . . . .	19
4.3	KM3NeT . . . . .	21
<b>5</b>	<b>Characteristics of PMTs</b>	<b>25</b>
5.1	Photocathode . . . . .	25
5.2	Dynode System . . . . .	26
5.3	Anode Sensitivity . . . . .	27
5.4	Single Electron Spectrum . . . . .	28
5.5	Timing . . . . .	29
5.6	Dark current . . . . .	30
<b>6</b>	<b>PMT candidates for the KM3NeT project</b>	<b>31</b>
6.1	ETEL D783KFLA . . . . .	31
6.2	Hamamatsu R12199-02 . . . . .	31
<b>7</b>	<b>Installation of a detection efficiency measurement test bench</b>	<b>33</b>
7.1	Measurement principle . . . . .	33
7.2	Design of the test bench . . . . .	35
7.3	Light field . . . . .	37
7.4	Calibration of the diaphragms . . . . .	39
7.5	Measurement of waveforms with the PMT . . . . .	41
7.6	Calculation of the detection efficiency . . . . .	42
7.7	Measurement with the Hamamatsu PMT . . . . .	45
<b>8</b>	<b>Quantum efficiency measurement</b>	<b>49</b>
8.1	Measurement principle . . . . .	49
8.2	Quantum efficiency scan . . . . .	49

<b>9</b>	<b>Improvement of the test bench</b>	<b>55</b>
9.1	Protective tube . . . . .	55
9.1.1	Tube simulation . . . . .	56
9.1.2	Measurements with the improved tube . . . . .	59
9.2	Calibration of the diaphragm . . . . .	62
9.3	Design of the improved test bench . . . . .	63
9.4	Error calculation . . . . .	64
9.5	Measurements with the improved test bench . . . . .	66
9.6	Linear Scan . . . . .	67
<b>10</b>	<b>Summary and Outlook</b>	<b>69</b>
	<b>List of Figures</b>	<b>71</b>
	<b>List of Tables</b>	<b>73</b>
	<b>Bibliography</b>	<b>75</b>

# Chapter 1

## Motivation

Photomultiplier tubes (PMTs) are the eyes of many detectors that concentrate on the measurement of low fluxes of light. As the KM3NeT detector, for which this thesis is done, is planned to measure neutrinos indirectly via the Cherenkov radiation of charged particles in water, it is very important to find the best PMTs for this kind of detector and to characterize them very well. At the Erlangen Centre for Astroparticle Physics (ECAP), strong effort is put into investigating different kinds of PMTs that are possible candidates to be used in the KM3NeT project. KM3NeT is a planned underwater neutrino telescope. Its line of sight will point towards the southern hemisphere, expanding the presence of ANTARES as underwater Cherenkov detector in the Mediterranean Sea and complementing the Ice Cube detector at the south pole, buried in ice, the line of sight of which points towards the northern hemisphere. The size of KM3NeT will exceed that of the existing detectors. In some of the proposed models, the instrumented volume will exceed six cubic kilometres. The field of research of KM3NeT ranges from Dark Matter to distant point sources like Active Galactic Nuclei, Gamma Ray Bursters, Supernovae and Colliding Stars.

The concrete aim of this thesis is the characterization of the optical properties of the PMT candidates for the Digital Optical Modules (DOMs) of KM3NeT, using an existing test bench to measure the Quantum Efficiency (QE) and building up a new test bench to measure the Detection Efficiency (DE) and hence to calculate the Collection Efficiency (CE). These parameters are essential input for the track reconstruction of charged particles originating from neutrino interactions, and thus help to estimate the energy and direction of the neutrino itself.

The basic elements of neutrino astronomy, like cosmic rays, neutrino sources, neutrino production mechanisms and interaction of neutrinos with matter and light fields, are discussed in this thesis. Furthermore, the Cherenkov effect, detection methods with telescopes like KM3NeT and their construction design will be presented. A muon with a velocity  $v = c$  emits roughly 400 photons per cm in water in the wavelength range from 300 – 700 nm. The mean distance between the DOMs is of the order of 100 m and the maximum absorption length in water for the mentioned wavelength regime is roughly 70 m. Those numbers show that an underwater neutrino telescope like KM3NeT has to deal with very small amounts of light. Therefore, the detection principle of small numbers of photons with PMTs and the important characteristic properties will be discussed. Promising types of photomultiplier tubes from the companies Hamamatsu Photonics and Electron Tubes Enterprises Ltd. are presented. The main part of this thesis deals with the construction of a detection efficiency measurement test bench. Detection efficiency and quantum efficiency measurements are made, the results allow for the calculation

of the collection efficiency of a PMT. In addition, their angular acceptance is investigated.

# Chapter 2

## Cosmic rays

Divulging information about some of the highest energy processes in the universe, cosmic rays are very important messengers of physics outside of the earth. The origins of cosmic rays are very manifold and thus their energy spectrum is very broad. The sources of cosmic rays accelerate charged particles with different mechanisms. The charged part of primary cosmic rays measured at the earth consists of roughly 99 % nuclei and 1 % electrons. The chemical composition of the nuclei part of the primary cosmic rays consist of roughly 85 % protons and 12 %  $\alpha$  particles. The remaining 3 % are elements with charge number  $Z \geq 3$ . The energy spectrum of the cosmic rays, shown in figure 2.1 provides information about how many particles are measured at different energies. As figure 2.1 shows, the spectrum follows a broken power law, which is separated in three main parts. The first part till around  $5 \cdot 10^6$  GeV, where the so called knee emerges, almost only consists of cosmic rays of galactic origin. The galactic sources are for example the sun, supernovae and their remnants, pulsars and micro quasars. As most theories predict highest energies of cosmic rays of galactic sources of up to  $10^8$  GeV, the most probable explanation for the knee is the galactic containment theory. This theory says that for the magnetic field of our galaxy ( $B \approx 10^{-10}$  T) protons with energies of above  $5 \cdot 10^6$  GeV start to escape from the galaxy. This energy depends indeed on the charge of the particle and so is greater for heavier nuclei. The fact that above this threshold ever less cosmic ray particles reach the earth explains the steepening of the spectrum from power index  $\gamma \approx 2.7$  to  $\gamma \approx 3.2$ . When the ankle appears at energies of about  $10^{10}$  GeV, the extragalactic component of the cosmic rays begins to dominate. This causes a flattening of the spectrum with power index  $\gamma \approx 2.8$ . Extragalactic sources are for instance gamma ray bursts, active galactic nuclei and hypernovae. Upwardly the spectrum is limited to energies of about  $6 \cdot 10^9$  GeV. This limit is named the Greisen-Zatsepin-Kuzmin (GZK) cutoff and is caused by the production of pions, when protons react with the cosmic microwave background photons via the  $\Delta$ -resonance:

$$\gamma + p \rightarrow p + \pi^0, \quad \gamma + p \rightarrow n + \pi^+ \quad (2.1)$$

The proton energy of this threshold is calculated as follows:

$$E_p = (m_\pi^2 + 2m_p m_\pi)/4E_\gamma \quad (2.2)$$

This equation results from the four-momentum conservation, where  $m_\pi$  is the pion mass,  $m_p$  the proton mass and  $E_\gamma$  is the energy of the photons of the cosmic microwave background, with a blackbody radiation temperature of 2.7 K,  $E_\gamma = 1.1$  meV. This leads to the energy  $E_p \approx 6 \cdot 10^9$  GeV. The mean free path of protons with this energy is about 10 Mpc. As this high

energies can not be produced in or near our galaxy, cosmic rays with energies far above the GZK-cutoff should not reach the earth.

In addition to the primary cosmic rays, every new particle formed in reactions with the primaries is a part of the secondary cosmic rays. The reactions can be performed in the source itself, in matter or photon fields being located in the direction, the particle travels, or in the atmosphere of the earth. Figure 2.2 shows the composition of the cosmic ray spectrum from different sources. The KM3NeT experiment, described in section 4.3, will be sensitive in an energy range from a few GeV up to the GZK cutoff.

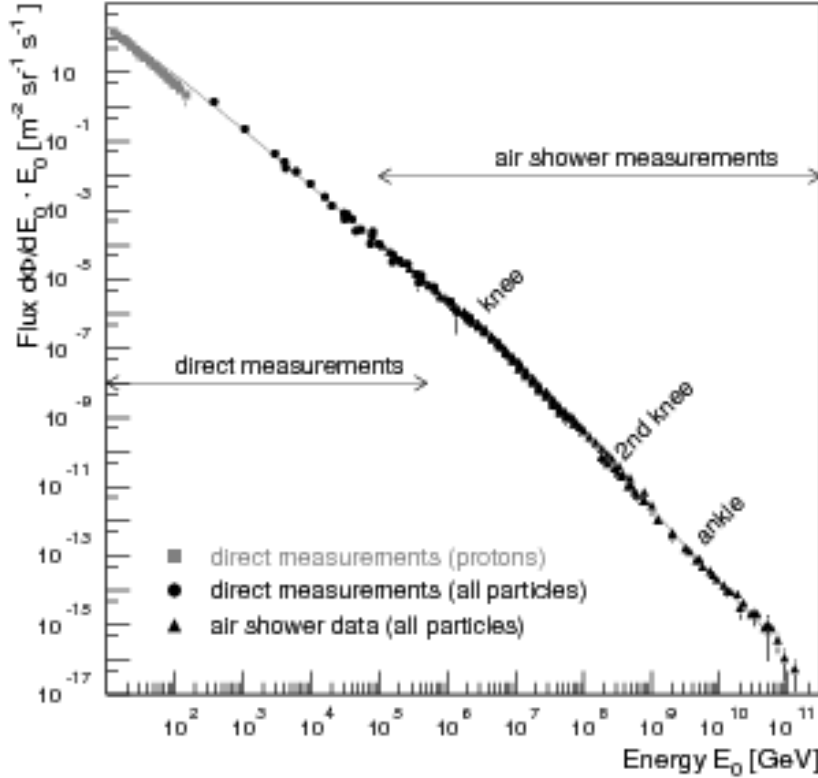


Figure 2.1: Energy spectrum of cosmic rays, figure taken from [1]

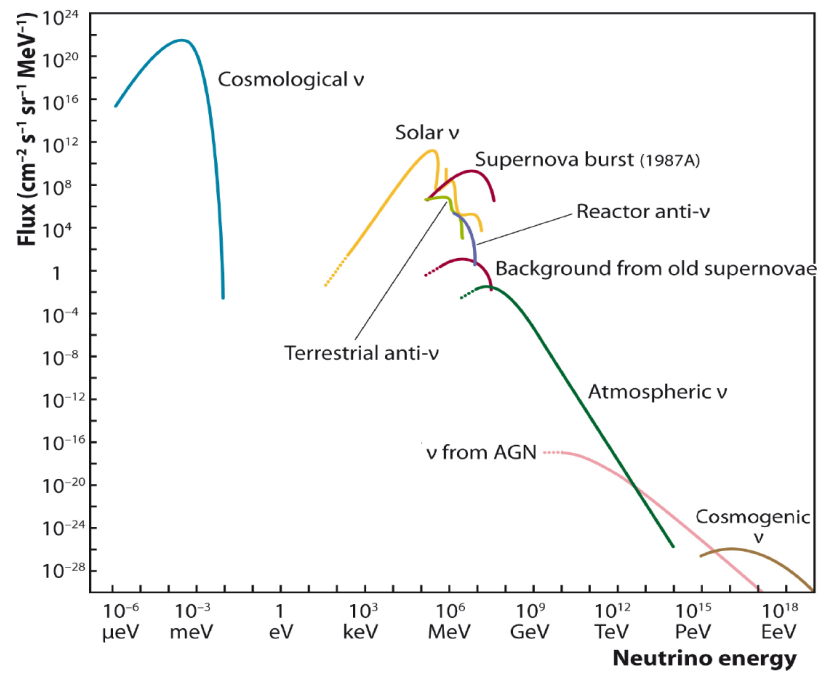


Figure 2.2: Sources of cosmic rays, figure taken from [1]





# Chapter 3

## Neutrinos

In this chapter, characteristics of neutrinos are explained and their suitability as messengers for highest energy processes in the universe is pointed out.

As written in [2], there are “requirements for an optimal astronomy”. Galactic or extragalactic magnetic fields should not distract the particle. This excludes charged particles like electrons or protons. The life time of the particle should exceed the time needed to travel from the source to the earth, which excludes neutrons with a life time of the order of  $10^3$  s. Even with the highest energies, and taking the time dilation into account, neutrons can not travel much further than a few megaparsecs. Another requirement is that the particle should not be its own antiparticle, which excludes photons as  $\gamma = \bar{\gamma}$ . With this distinction one can determine whether the nature of the source, the particle comes from is of matter or antimatter. The last point is that the particle has to have a small cross section for the interaction with the source itself or e.g. interstellar gas, so it can travel without obstacles and can deliver information of the inside of the source and not just from the surface. Neutrinos can fulfil these requirements but mainly the last point makes it very challenging to measure them.

### 3.1 Neutrino production

As mentioned in chapter 2, the energy cosmic rays gain originates from acceleration of charged particles. Neutrinos have no charge and so they have to be produced in reactions of the charged particles with matter or fields.

**Atmospheric neutrinos** emerge when protons collide with nuclei of the air and produce hadronic showers. Besides many other reaction products, charged pions can be produced:

$$p + X \rightarrow \pi^{\pm,0} + X^* \quad (3.1)$$

The pions itself decay after a short time into muons and muon neutrinos:

$$\pi^+ \rightarrow \mu^+ + \nu_\mu \quad , \quad \pi^- \rightarrow \mu^- + \bar{\nu}_\mu \quad (3.2)$$

After that, the unstable muons decay into electrons and neutrinos:

$$\mu^+ \rightarrow e^+ + \nu_e + \bar{\nu}_\mu \quad , \quad \mu^- \rightarrow e^- + \bar{\nu}_e + \nu_\mu \quad (3.3)$$

This reaction chain can also happen with kaons instead of pions. Atmospheric neutrinos can have energies from about a few MeV up to  $10^6$  GeV.

**Supernovae neutrinos** are produced during the gravitational collapse of a massive star in consequence of the deleptonization. Electrons and protons react to neutrons and electron neutrinos:

$$e^- + p \rightarrow n + \nu_e \quad (3.4)$$

Furthermore, due to the high temperature in supernovae, thermal photons can produce electron-positron pairs, which can produce neutrinos via the weak interaction, where a virtual  $Z$  is produced by the electron-positron pair and decays into a neutrino and an antineutrino:

$$e^+ + e^- \rightarrow Z \rightarrow \nu_l + \bar{\nu}_l \quad (3.5)$$

The mean energy of supernova neutrinos is  $\approx 15$  MeV.

**High energy neutrinos** are produced in supernova remnants, gamma ray bursts, active galactic nuclei or via the GZK-cutoff. The production mechanisms are proton-proton interaction as described for atmospheric neutrinos above in equations 3.1, 3.2 and 3.3 and proton-photon interactions with the cosmic microwave background or infrared or ultraviolet photon fields via the delta resonance. The neutrinos produced in the GZK cutoff are also called cosmogenic neutrinos.

$$p + \gamma \rightarrow \Delta^+ \rightarrow \begin{cases} \pi^+ + n \\ \pi^0 + p \end{cases} \quad (3.6)$$

The pions, as products of this reaction then decay to neutrinos as in equations 3.2 and 3.3. Figure 3.1 shows a possible cosmogenic neutrino flux of the described proton-photon interactions with the cosmic microwave background (CMB) or infra red (IR) to ultra violet (UV) photon fields [2].

## 3.2 Neutrino interaction

The cross section of neutrinos for baryonic interactions is very low over the whole energy range of the cosmic ray spectrum. Nevertheless, there are some interactions neutrinos can cause with particles at the earth.

The **neutrino-nucleon interactions** are weak interactions and occur when a neutrino hits a nucleus ( $N$ ). Charged current (CC) and neutral current (NC) interactions can occur:

$$\bar{\nu}_l + N \rightarrow W^\mp \rightarrow l^\mp + X \quad (\text{CC}) \quad (3.7)$$

$$\nu_l + N \rightarrow Z^0 \rightarrow \nu_l + X \quad (\text{NC}) \quad (3.8)$$

Figure 3.2 shows the cross section of neutrino-nucleon CC and NC interactions for high energy neutrinos. The only additional non neutrino-nucleon interaction that is relevant, regarding the cross section, is the **Glashow resonance**. The Glashow resonance occurs when the energy of an electron neutrino is high enough to produce a  $W^-$  by hitting an electron:

$$\bar{\nu}_e + e^- \rightarrow W^- \rightarrow \begin{cases} \bar{\nu}_l + l^- \\ q + \bar{q} \end{cases} \quad (3.9)$$

$q$  and  $\bar{q}$  can be any quark and anti quark pair.

Figure 3.3 shows the Glashow resonance of the neutrino-electron interaction and its peak at  $6.3 \cdot 10^6$  GeV. At that energy, the neutrino-electron interaction becomes relevant [2].

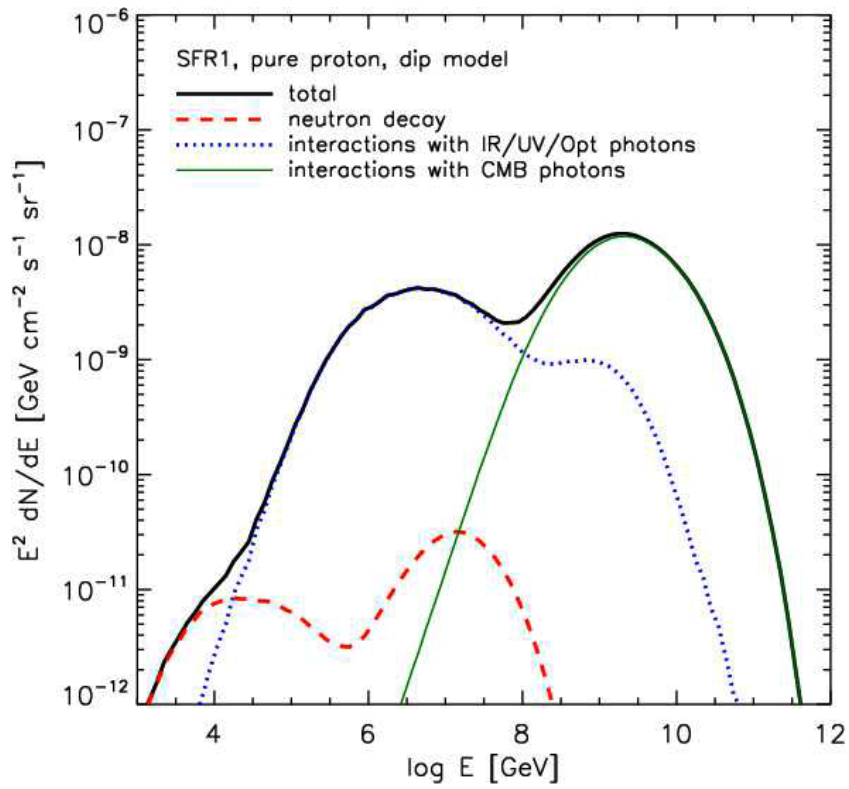


Figure 3.1: Possible cosmogenic neutrino flux from proton-photon interaction with the CMB or IR/UV photons, figure taken from [3].

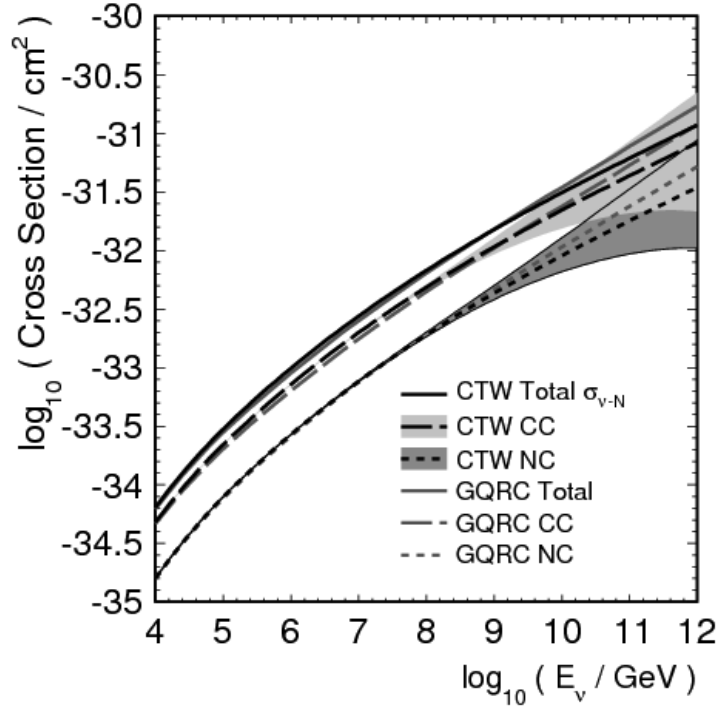


Figure 3.2: High energy neutrino-nucleon CC and NC cross section, figure taken from [4].

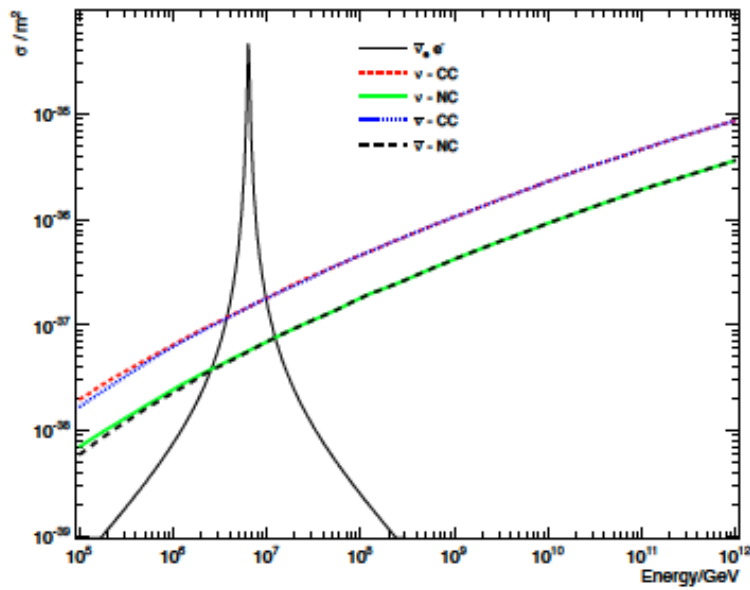


Figure 3.3: Glashow resonance of neutrino-electron interaction, figure taken from [5].

# Chapter 4

## Underwater neutrino telescopes

In this chapter, the principles of neutrino detection in underwater neutrino telescopes are presented and the existing ANTARES telescope and the planned KM3NeT telescope are introduced.

As mentioned in chapter 3, the cross section of interactions of neutrinos with matter is very small. Therefore, the volume of the medium for interaction has to be as large as possible. The detector uses the water or the bedrock below as media. With the aforementioned reactions (section 3.2), charged particles are produced, for example a muon. If this muon travels through the water with a velocity faster than the phase velocity of light, Cherenkov light is produced and can be measured by the optical detectors which are installed underwater in the deep sea.

### 4.1 Cherenkov radiation

The Cherenkov effect describes the emission of photons when a charged particle travels through a medium with a velocity  $v$  higher than the speed of light in the medium with refractive index  $n$ :

$$v \geq \frac{c}{n} \quad (4.1)$$

The angle of emittance of the radiation relative to the travel direction of the charged particle is:

$$\theta_C = \arccos \frac{1}{n\beta}, \quad (4.2)$$

where  $\beta = v/c$ .

Figure 4.1 shows a Cherenkov cone caused by a muon and a spherical Cherenkov front resulting from a hadronic or electromagnetic cascade in a detector. The Cherenkov spectrum, a charged particle causes is expressed in number of emitted photons  $N$  per path length  $dx$  and wavelength intervall  $d\lambda$ :

$$\frac{dN}{dx d\lambda} = \frac{2\pi \cdot z^2 \alpha}{\lambda^2} \left( 1 - \frac{1}{\beta^2 \cdot n^2(\lambda)} \right) \quad (4.3)$$

$z$  is the charge of the particle in units of the elementary charge  $e$  and  $\alpha \approx \frac{1}{137}$  is the fine structure constant.

As  $n(\lambda)$  is assumed to be nearly constant ( $n \approx 1.33$ ) in the wavelength regime where the water is transparent for photons (see also table 4.1), the formula above can be integrated over  $\lambda$ :

$$\frac{dN}{dx} = 2\pi \cdot z^2 \alpha \left( 1 - \frac{1}{\beta^2 \cdot n^2} \right) \int_{\lambda_1}^{\lambda_2} \frac{1}{\lambda^2} d\lambda \quad (4.4)$$

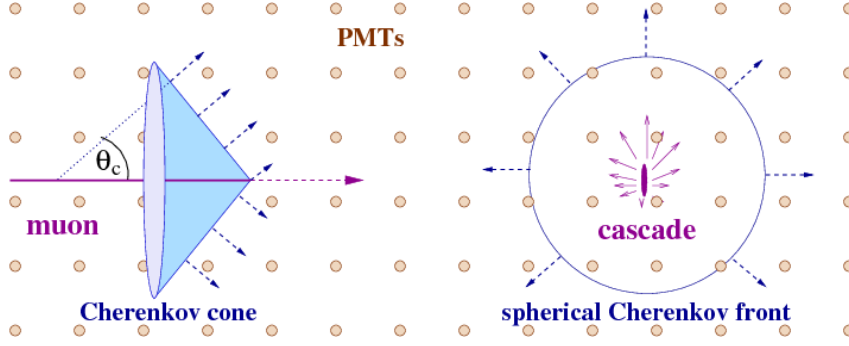


Figure 4.1: Schematic picture of a Cherenkov cone caused by a muon and a spherical Cherenkov front for instance caused by a shower in a detector, figure taken from [1].

The number of photons emitted per path length is:

$$\frac{dN}{dx} = -2\pi \cdot z^2 \alpha \left(1 - \frac{1}{\beta^2 \cdot n^2}\right) \cdot \left(\frac{1}{\lambda_2} - \frac{1}{\lambda_1}\right) \quad (4.5)$$

According to this formula, a muon with a velocity of  $v = c$  emits roughly 400 photons per cm in the wavelength region from 300 – 700 nm. Table 4.1 shows the absorption length  $L_a$  and

$\lambda$ [nm]	$L_a$ [m]	$L_s$ [m]
290	0.0	16.6
310	11.9	20.2
330	16.4	23.8
350	20.6	27.6
375	29.5	32.5
412	48.5	40.2
440	67.5	46.2
475	59.0	53.9
488	55.1	56.8
510	26.1	61.8
532	19.9	66.8
555	14.7	72.1
650	2.8	94.2
676	2.3	100.3
715	1.0	109.4
720	0.0	109.4

Table 4.1: Absorption length  $L_a$  and scattering length  $L_s$  of light for different wavelengths  $\lambda$  in water, values taken from [6]

scattering length  $L_s$  for photons of different wavelengths  $\lambda$  in water. The numbers of unabsorbed  $N_a$  and unscattered  $N_s$  photons in a distance  $d$  are calculated as follows:

$$N_a = N_0 \cdot e^{-\frac{d}{L_a}} \quad , \quad N_s = N_0 \cdot e^{-\frac{d}{L_s}} \quad (4.6)$$

Assuming, that scattered photons are scattered away and don't reach the detection unit, the transmission of water  $T$  can be calculated:

$$T = A \cdot S, \quad (4.7)$$

with  $A = \frac{N_a}{N_0}$  and  $S = \frac{N_s}{N_0}$ .

Table 4.2 shows the transmission coefficient  $T$  calculated with the values of table 4.1 and equation 4.7, the relative number  $N_{CS}$  of photons emitted via the cherenkov effect for different wavelengths and the multiplication of each of the values as the relative spectrum arriving at the detection units. The PMTs have to be sensitive in this wavelength region and as it can be seen in figure 5.2, there is a good agreement between the quantum efficiency of the PMT and the spectrum arriving at the detection units. Figure 4.2 shows the relative transmission of water and the multiplication with the cherenkov spectrum.

$\lambda$ [nm]	$T$	$N_{CS}$	$T \cdot N_{CS}$
290	0	1.00	0
310	$1.59 \cdot 10^{-6}$	0.875	$1.39 \cdot 10^{-6}$
330	$3.38 \cdot 10^{-5}$	0.772	$2.61 \cdot 10^{-5}$
350	$2.08 \cdot 10^{-4}$	0.687	$1.43 \cdot 10^{-4}$
375	$1.55 \cdot 10^{-3}$	0.598	$9.27 \cdot 10^{-4}$
412	$1.06 \cdot 10^{-2}$	0.495	$5.25 \cdot 10^{-3}$
440	$2.61 \cdot 10^{-2}$	0.434	$1.13 \cdot 10^{-2}$
475	$2.87 \cdot 10^{-2}$	0.373	$1.07 \cdot 10^{-2}$
488	$2.80 \cdot 10^{-2}$	0.353	$9.88 \cdot 10^{-3}$
510	$4.30 \cdot 10^{-3}$	0.323	$1.39 \cdot 10^{-3}$
532	$1.47 \cdot 10^{-3}$	0.297	$4.37 \cdot 10^{-4}$
555	$2.78 \cdot 10^{-4}$	0.273	$7.59 \cdot 10^{-5}$
650	$1.07 \cdot 10^{-16}$	0.199	$2.13 \cdot 10^{-17}$
676	$1.37 \cdot 10^{-44}$	0.184	$2.52 \cdot 10^{-45}$
715	0	0.165	0
720	0	0.162	0

Table 4.2: Transmission coefficient  $T$  in a distance of  $d = 100$  m, the relative number of emitted photons via the cherenkov effect and the multiplication of each of the values.

## 4.2 ANTARES

The ANTARES (Astronomy with a Neutrino Telescope and Abyss environmental RESearch) telescope is located in the mediterranean deep sea 40 km off the French cost near Toulon. At a depth of about 2500 m, 12 strings with length 450 m are at the one end anchored in the ground and at the other end pulled upwards by buoys. Each string consists of 25 storeys, of which each consists of three optical modules. The optical modules point downwards  $45^\circ$  relative to the strings and house a Hamamatsu 10-inch Photomultiplier tube (PMT) each, which is responsible for the detection of the Cherenkov light. The Cherenkov light measured with more than one optical module allows for the reconstruction of the track of the fast charged particle which induced the Cherenkov light. When the direction is upwards, the high energy charged particle has been produced by a neutrino interacting with the matter around the detector. With this technique it is possible to detect neutrino point sources.

In addition, acoustic modules have been installed at two strings to detect the pancake like sound wave, ultra high energy (UHE) neutrino induced showers cause by depositing energy in the

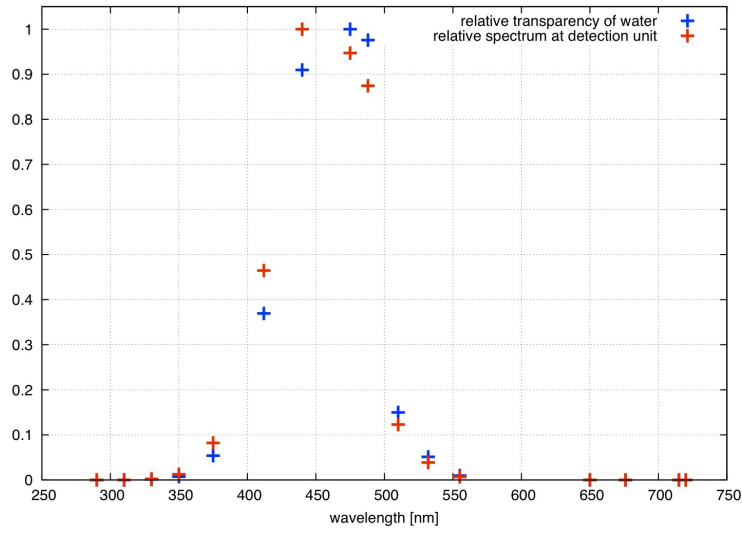


Figure 4.2: Relative transparency of water (blue crosses) and the multiplication with the cherenkov spectrum (red crosses).

water surrounding the detector. Figure 4.3 shows a schematic picture of the ANTARES detector [7].

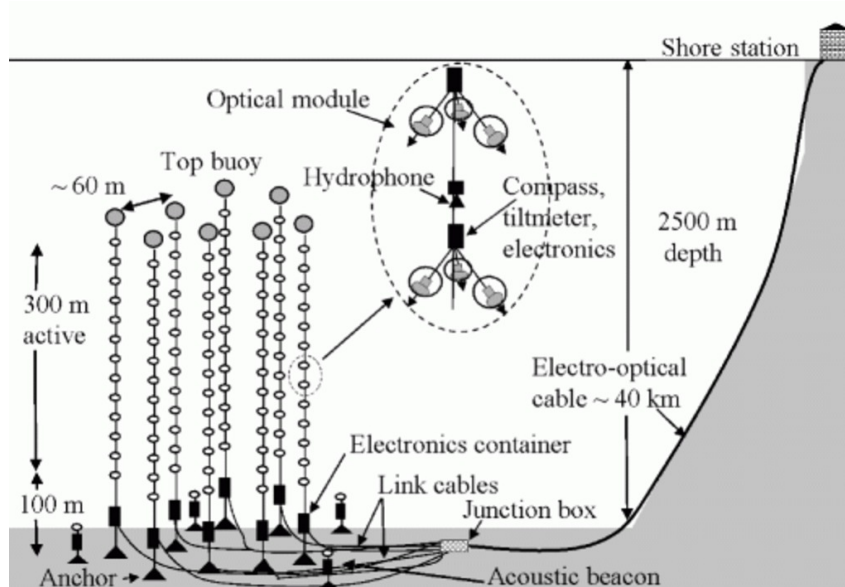


Figure 4.3: Schematic picture of the ANTARES detector, figure taken from [7].



### 4.3 KM3NeT

KM3NeT is a multi  $\text{km}^3$  sized neutrino telescope, which is planned to be built at the ground of the Mediterranean Sea. Probable sites are Toulon, Capo Passero and Pylos, see figure 4.4. The scientific goal is the search for astrophysical neutrino sources inside and outside of our galaxy, as described in chapter 2. Additional goals will be earth and marine science and to find dark matter in the universe. Many experiences of the pioneer projects ANTARES, NEMO and NESTOR can be brought into the design, construction and operation phase of KM3NeT.

The principle idea of the telescope is similar to that of ANTARES. The goal is to detect diffuse flux neutrinos and neutrinos from point sources by measuring the Cherenkov light, that charged particles, that were produced in interactions with matter, cause in the seawater (see section 4.1). The structure of the detector, according to current state, consist of 320 nearly one km long strings anchored in the ground called detection units (DU), which house 20 digital optical modules (DOM) (see figure 4.6) in equal distances. The DUs put up, with distances of 150 – 180 m from each other, an instrumented volume of roughly six  $\text{km}^3$ . The DOM consists of a glass sphere which houses 31 three inch photomultiplier tubes (PMT) which measure the Cherenkov light and convert it into an electric signal, that is read out and converted by the electronic board which is also installed in the glass sphere. The signals from the different DOMs are collected with fibers and transported to the shore, where they are further processed. In this configuration, the detector consists of 396800 PMTs and 12800 DOMs.

The new multi PMT DOMs can perform a better directional reconstruction than for instance the optical modules of ANTARES which house only one 10 inch PMT. The lower energy threshold for detectable neutrinos is about a few 100 GeV. For neutrino energies of more than 10 TeV the angular resolution of KM3NeT is better than  $0.1^\circ$ . Further informations about the layout and the performace of the detector can be found in the technical design report [8].

Figure 4.5 shows an artist view of the KM3NeT detector layout.

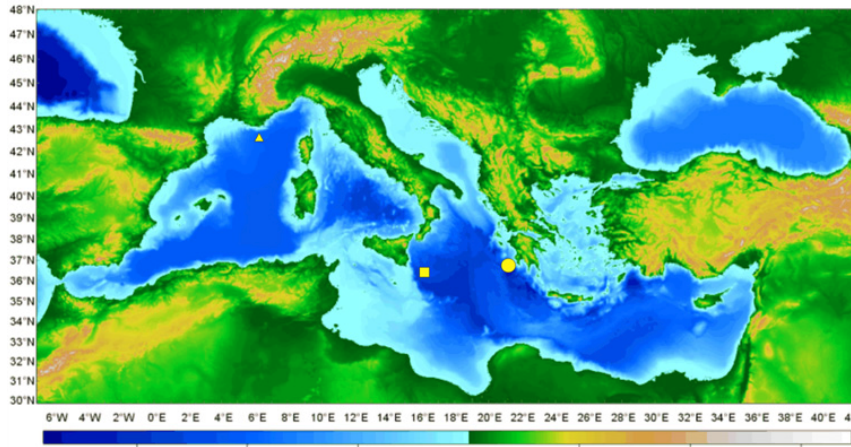


Figure 4.4: Possible sites for the installation of the detector, triangle for Toulon, rectangle for Capo Passero and circle for Pylos, figure taken from [8].

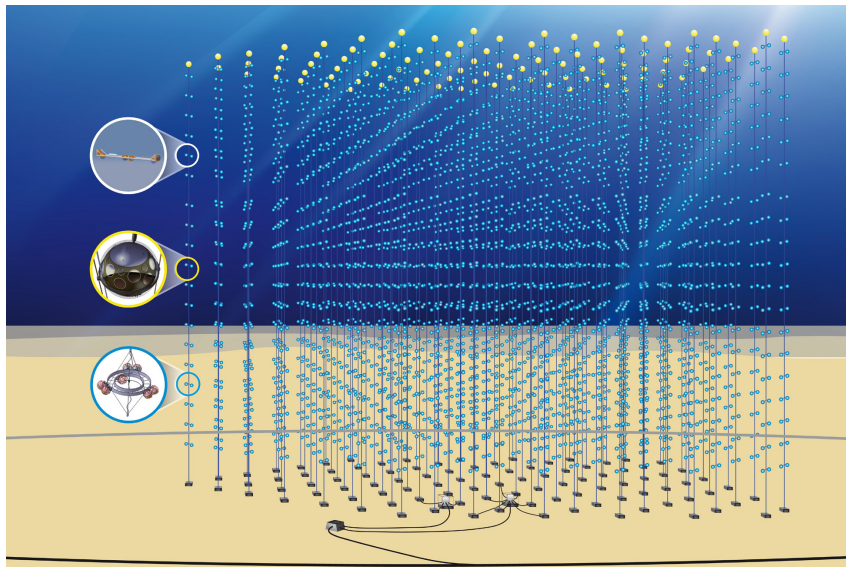


Figure 4.5: Artist view of the KM3NeT detector, figure taken from [8].

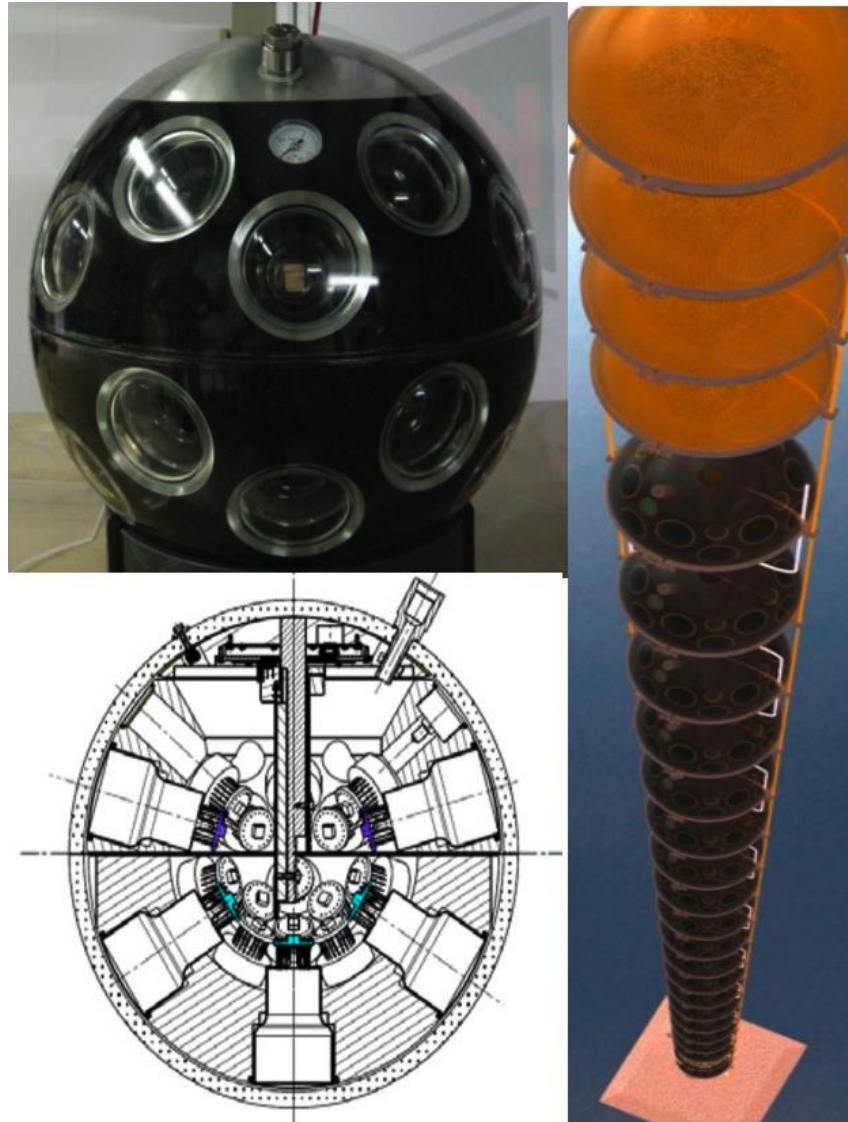


Figure 4.6: Real (top left) and schematic picture (bottom left) of the KM3NeT DOM and a string with many DOMs (right), figures taken from [9] and [8].



# Chapter 5

## Characteristics of PMTs

This chapter contains information about Photomultiplier tubes, its operating principle and its components. As mentioned in chapter 1, PMTs are powerful instruments for detecting small amounts of light. The measuring principle is to catch the light, transform it into electrons that are multiplied to a quantity that can be measured as a flowing current. The typical schematic composition of a PMT is shown in Figure 5.1. It is an evacuated tube with a photocathode at its faceplate. If a photon hits the faceplate and hence the photocathode, there is a chance to release an electron via the photoelectric effect. This electron is then focused and accelerated towards the dynode system, as the photocathode lies on high negative potential, which is decreasing step by step with the dynodes. The dynode system consists of mostly about 10 dynodes, at each dynode one electron is multiplied by secondary emission. The total amplification, thus, follows a power law which depends on the secondary coefficient and the number of dynodes. After the amplification process, the electrons can be collected by the anode. Standard operating voltages reach from 1000 to 1500 V between the photocathode and the anode.

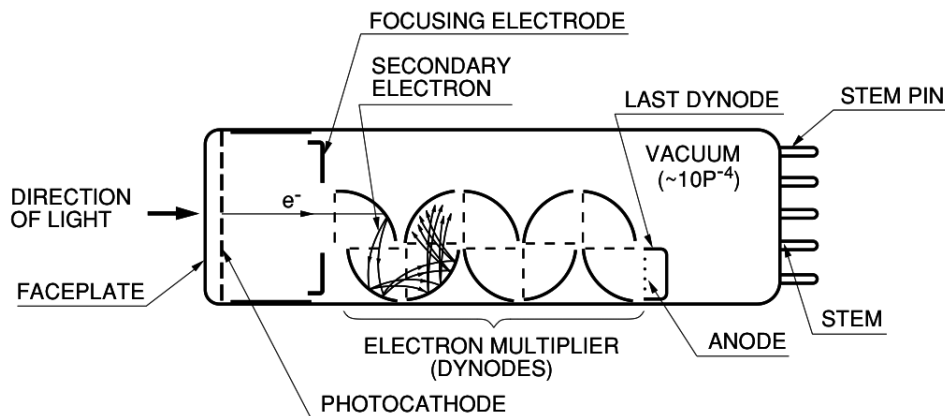


Figure 5.1: Schematic picture of a PMT, taken from [10]

### 5.1 Photocathode

Photocathodes mostly consist of bi- or trialkali materials as SbKCs or SbRbCs. The sensitivity of the photocathode depends on its thickness and chemical composition and on the wavelength of the incident light. It is limited in the infra red region by the photoemission threshold and in

the UV region by the transmission of the glass used for the tube. The photoemission threshold is the energy, an electron needs to escape from the material. The absorbed energy of an incident photon before is reduced by losses during diffusion through the material. The photocathode sensitivity  $S_c$  is often expressed in radiometric units by the manufacturers:

$$S_c = \frac{I_c}{\Phi}, \quad (5.1)$$

where  $\Phi$  is the incident flux and  $I_c$  is the photocathode current less the dark current. To get the spectral sensitivity,  $d\Phi$  is defined as the increment flux in a wavelength increment  $d\lambda$ , causing the photocathode current increment  $dI_c$ . The spectral sensitivity is given by:

$$S_{c,\lambda} = \lim_{d\lambda \rightarrow 0} \frac{dI_c}{d\Phi} \quad (5.2)$$

In the content of this work the Quantum Efficiency (QE) is exclusively used as a degree of Sensitivity. The quantum efficiency is defined as follows:

$$QE = \frac{\text{emitted photoelectrons}}{\text{incident photons}} \quad (5.3)$$

and can be expressed via the spectral sensitivity  $S_{c,\lambda}$ :

$$QE(\lambda) = S_{c,\lambda} \cdot \frac{hc}{\lambda e}, \quad (5.4)$$

where  $h$  is the planck constant,  $c$  is the speed of light in vacuum and  $e$  is the elementary charge. The quantum efficiency can be measured by shortcutting the focus dynode with the dynode system and the anode, removing the amplification but collecting nearly all electrons emerging out of the photocathode and measuring the current induced by them. As a reference, a current measurement with a Photodiode (PHD) with known quantum efficiency is done under the same conditions for each wavelength. The spectral quantum efficiency of the PMT can be calculated as follows:

$$QE_{PMT}(\lambda) = QE_{PHD}(\lambda) \cdot \frac{I_{PHD}(\lambda)}{I_{PMT}(\lambda)}, \quad (5.5)$$

where  $QE_{PHD}$  is the quantum efficiency of the PHD and  $I_{PHD}$  and  $I_{PMT}$  are the measured currents of the PHD and the PMT.

Figure 5.2 shows a measured spectral quantum efficiency of a PMT from the company ET Enterprises LTd. (ETEL).

## 5.2 Dynode System

The ratio between the electrons arriving at the first dynode and the electrons emitted from the photocathode  $n_c$  is called the collection efficiency (CE). It depends primarily on the electron optics, that means on the focusing of the emitted electrons from the photocathode to the first dynode. This depends on the design of the PMT and on the electric field between the photocathode and the first dynode. Another effect that can influence the collection efficiency is the elastic scattering of electrons at the first dynode.

The Gain  $G$ , as it is often defined by manufacturers, is the ratio between the anode current  $I_a$

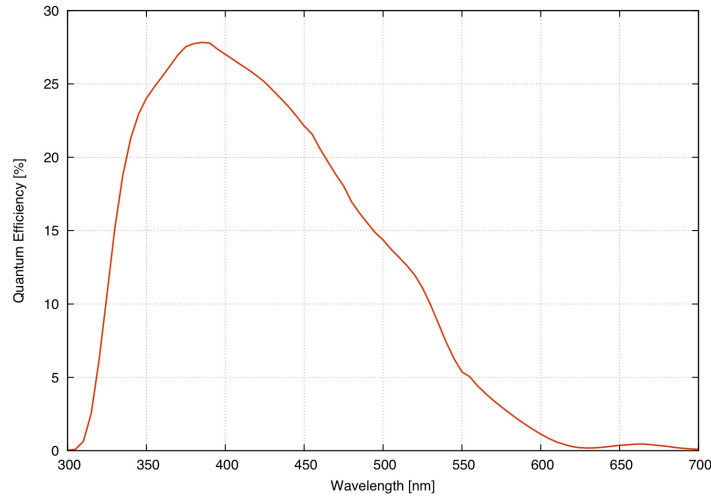


Figure 5.2: Measured spectral quantum efficiency of an ETEL PMT

and the photocathode current  $I_c$  and includes the amplification of the dynode system. At each dynode emerges secondary emission which leads to an exponential increase of the number of electrons in the system. The amount of electrons that reach the anode ( $n_a$ ) is:

$$n_a = n_c \cdot G = n_c \cdot CE \cdot \prod_{i=1}^N \delta_i \eta_i = CE \cdot \prod_{i=1}^N g_i, \quad (5.6)$$

where  $\delta_i$  is the secondary emission coefficient for each dynode,  $\eta_i$  is the collection efficiency between the  $i$ -th and the  $(i + 1)$ -th dynode,  $g_i$  is the gain of each stage and  $N$  is the total number of dynodes including the anode. In this definition, the measured currents at the photocathode and at the anode are used to calculate the gain. In the content of this work another definition of the gain and the collection efficiency are used. The gain is measured with a single electron spectrum, as described in section 5.4. The measured charge of the single electron peak is divided by the elementary charge to calculate the amplification. This amplification should be the gain without the factor of the collection efficiency. The used high voltage to achieve a characteristic amplification of  $5 \cdot 10^6$  is lower than it is for the definition in equation 5.6.

### 5.3 Anode Sensitivity

The anode sensitivity can be described similar as the photocathode sensitivity by the ratio between the current and the incident flux:

$$S_a = \frac{I_a}{\Phi} \quad (5.7)$$

Similar to the spectral photocathode sensitivity the spectral anode sensitivity can be expressed by:

$$S_{a,\lambda} = \lim_{d\lambda \rightarrow 0} \frac{dI_a}{d\Phi} \quad (5.8)$$

Considering the gain it can also be express by the photocathode sensitivity:

$$S_a = S_c \cdot G \quad (5.9)$$

In this work the detection efficiency (DE) is an important issue. It is defined as the product of the collection efficiency and the quantum efficiency. For small wavelength steps it can be written:

$$DE(\lambda) = CE(\lambda) \cdot QE(\lambda) \quad (5.10)$$

The measurement technique of the detection efficiency covers a big part of this work and it is explained in detail in chapter 7.

## 5.4 Single Electron Spectrum

If the light source to be measured with a PMT has low intensity, single photoelectrons are detected. They can be measured in different ways. In this work the PMT is connected to an oscilloscope and the signal waveforms that result from the incident light, which is a pulsed light with fixed frequency and pulse width, are saved and many parameters like the gain or time characteristics and a charge histogram can be derived from this informations. The histogram of charge is made by integrating the areas below the signal waveforms over the time. As there is a fixed integration window, every single pulse can be resolved and appearances like afterpulses can be suppressed because they emerge outside of the integration window. Afterpulses mainly occur if the residual gas in the tube is ionized by the electrons and hits the photocathode or when the electrons, hitting the dynodes, cause photons to emerge, that can hit the photocathode again etc. A more detailed description of afterpulsing can be found in [11]. For small incident light pulses, the resulting signals are clearly smaller than the time between signal and afterpulse (100 ns to a few  $\mu$ s). In this way, it is easy to eliminate the effect of afterpulsing. This is a difference between the waveform measurement and a current measurement, because at the current measurement all afterpulses are included in the measured current due to the integration time of the amperemeter.

The histogram of charge is made by integrating every single waveform in a fixed time window. The resulting charge values are used to make a binned histogram. Those histograms normaly show a spectrum with, mostly, huge pedestal which is the electronic noise. Additionally, some peaks with equivalent distances to each other can be identified. This are the  $n$ -electron peaks which can be resolved from one single to a few electrons. If the intensity of the light source is low enough ( mean number of photons per pulse of  $< 1$ ), it is possible to get a histogram with only the single electron peak. An example of such a single electron spectrum is shown in figure 5.3. The large pedestal and mainly one additional peak, which is the single electron peak can be identified.

This spectrum can provide useful information about the PMT. With the peak-to-valley ratio, the secondary emission coefficient can be estimated and with the mean value of the single electron peak the gain of the PMT can be determined, which is more detailed discussed in [11].

For this work it is important to know the mean measured number of photoelectrons per pulse. The number of photons emitted from the light source in a time window e.g. per pulse is poisson distributed. Thus the number of electrons arriving at the anode and so the charge of the pulse is poisson distributed, too.



The poisson distribution is given by:

$$P(k, \lambda) = \frac{\lambda^k \cdot e^{-\lambda}}{k!} \quad (5.11)$$

Here are  $k$  the number of electrons and  $\lambda$  the mean value of electrons.

To calculate the mean value of electrons per pulse, the formula for zero events in the poisson distribution

$$P(0, \lambda) = \frac{\lambda^0 \cdot e^{-\lambda}}{0!} \quad (5.12)$$

is resolved by  $\lambda$ :

$$\lambda = -\ln P(0, \lambda) \quad (5.13)$$

In this case, the probability of a zero event is given by the number of pedestal events ( $n_{ped}$ ) over the number of all events ( $n_{all}$ ) and therefore:

$$\lambda = -\ln \frac{n_{ped}}{n_{all}} \quad (5.14)$$

To get the parameter  $n_{ped}$  from the histogram of charge a threshold is set at the minimum between the pedestal peak and the single electron peak and the events with less charge are the pedestal events.

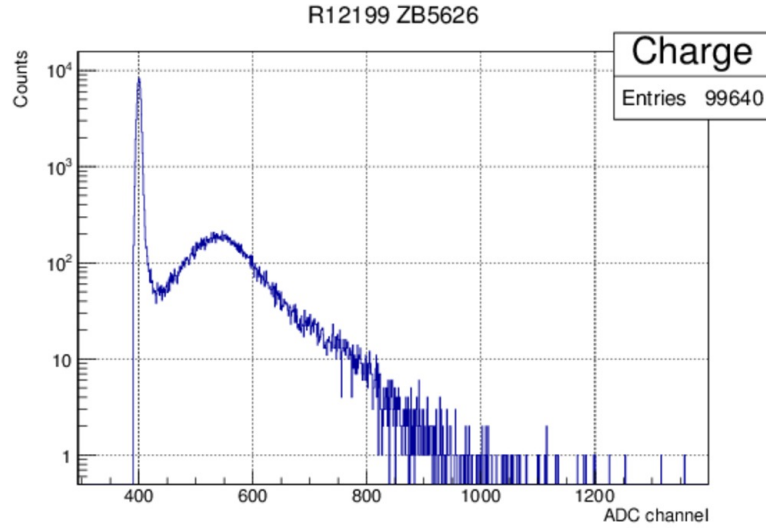


Figure 5.3: Measured histogram of charge with a single electron spectrum.

## 5.5 Timing

To complement the characteristics chapter some information about the timing of PMTs are given in this section. The response pulse width is the full width at half maximum (FWHM) of an anode signal of the PMT caused by an incident light pulse with a delta function shape. In reality, fast PMTs have response pulse widths of 2 – 4 ns with incident light pulse width of less than 1 ns.

The rise time is the time between the two points, when the anode signal exceeds 10 % and 90 % of the signal height. Its about 1 ns for PMTs with linear focusing dynodes.

The time between the incidence of the light pulse at the photocathode and the arrival of the signal at the anode is called the transit time (TT). It differs with the position, at which the light pulse hits the photocathode and with the applied voltage, which is in charge for the acceleration of the electrons.

The transit time spread (TTS) is defined as the FWHM of the distribution of the single transit times. If the PMT is irradiated with diffuse light pulses, the position of incidence at the photocathode varies and hence the TTS gets bigger because of the geometry of the electric field between the photocathode and the (focus)-dynodes (read more in [11]). The TTS is like the time resolution for PMTs and is a very important parameter to qualify a PMT.

## 5.6 Dark current

The dark current is the current, measured at the anode of a PMT that results not from light, hitting the photocathode. It results mainly from thermionic emission, leakage currents and field effects, but can also be effected by high energy photons e.g. by cosmic rays (see also [11]).

# Chapter 6

## PMT candidates for the KM3NeT project

In this chapter possible PMTs from different manufacturers for the KM3NeT experiment will be introduced. Hamamatsu Photonics and Electron Tubes Enterprises Ltd., both have good chances to get the contract for the mass production. In the preparation phase, different types of PMTs from both manufacturers were developed and tested for the properties that are important for the KM3NeT project, which are mainly those described in chapter 5.

### 6.1 ETEL D783KFLA

The ETEL D783KFLA is a 3 inch PMT from the British company ET Enterprises Ltd. (ETEL). The front window, coated with the photocathode material (bialkali) has a diameter of 77.8 mm. The radius of the outer curvature is 196 mm to fit in the glass sphere of the optical module with a diameter of 17 inch and the radius of the inner curvature is 67 mm. This configuration should guarantee same times of flight for the electrons from the photocathode to the first dynode and minimizes the transit time spread. The tube has a length of roughly 100 mm and the flying leads, the connectors to the photocathode, the different dynodes and the anode, have a length of roughly 85 mm. The box dynode system consists of 10 dynodes. Figure 6.1 shows a photo of the PMT.

### 6.2 Hamamatsu R12199-02

The Hamamatsu R12199-02 PMT is a 3 inch PMT and has a mushroom shaped front window. This minimizes the transit time spread as for the ET PMT, but is less expensive in the production than the lens system with the two different curvatures. The front window has a diameter of 80 mm and the radius of curvature is 50 mm. The total length of the tube is roughly 97 mm. It also has 10 dynodes in a box arrangement. Figure 6.2 shows a photo of the Hamamatsu R12199-02 PMT.



Figure 6.1: Photo of an ETEL D783KFLA PMT.



Figure 6.2: Photo of a Hamamatsu R12199-02 PMT.

# Chapter 7

## Installation of a detection efficiency measurement test bench

In this chapter the principle idea how to measure the detection efficiency in pulse mode is explained. Additionally, the design of a test bench that performs this measurements is described.

### 7.1 Measurement principle

The optical detection of the KM3NeT detector is performed by PMTs, so it is important to know how many of the incident photons can really be detected. As a muon produces only small amounts of cherenkov photons, that can be seen as light pulses in the detector, it is not very useful to measure the anode sensitivity with constant illumination, as it is done in most specifications. In addition, the electrons, produced by the incident light, are measured via an amperemeter, where the current, induced by the electrons, is integrated over time. In this case, there are several effects like afterpulsing that distorts the measurement. To bypass these effects, the detection efficiency is measured in pulse mode, where a LED is fed by short pulses from an Agilent 33220A Signal-Generator. The light pulses can be measured with the PMT while it is connected to an oscilloscope. If the number of photons per pulse is relatively small and if the oscilloscope triggers on the pulse of the signal generator, a signal from the PMT is seen if the pulse is detected, if not only the electronic noise is seen. The probability that the PMT measures a light pulse can be calculated by counting the number of signals and dividing them by the number of pulses produced by the frequency generator. If the window on the oscilloscope, where the signals emerge is integrated for every single event, a histogram of charge can be made as described in section 5.4. Figure 7.1 shows a histogram of charge with the drawn threshold in red. If the number of measured photoelectrons is poisson distributed, the mean number of photoelectrons per pulse  $N_{pe}$  can be calculated by counting the pedestal events (electronic noise) and all events and using the probability of a zero event in the poisson distribution as shown in section 5.4. The first peak in figure 7.1 is assigned to the pedestal and has a gaussian distribution. The second peak is the charge that corresponds to the charge of a single photoelectron after the amplification of the dynode system and is also gaussian distributed. As the mean number of photons per pulse was very small in this measurement, further peaks can be identified hardly, but the peaks are at equal distances to each other, the distance always matches the elementary charge times the amplification.

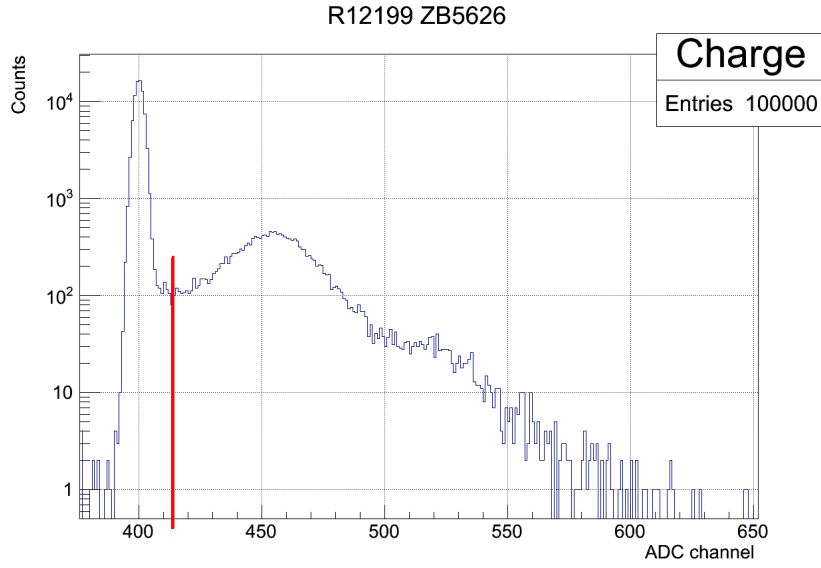


Figure 7.1: Histogram of charge with a threshold in red to calculate the mean number of photoelectrons per pulse

The absolute detection efficiency in pulse mode is defined as:

$$\text{absolute detection efficiency} = \frac{\text{number of measured photoelectrons per pulse}}{\text{number of photons per pulse}} \quad (7.1)$$

To measure the number of photons per pulse, a photodiode with known quantum efficiency  $QE_{PHD}$  is used. The photodiode current  $I_{PHD}$  is measured with an amperemeter. A photon hitting the detection area of the photodiode is converted to an electron with a probability equal to the quantum efficiency. The charge deposited in the amperemeter per second equals the measured current:

$$I_{PHD} = N_{ph} \cdot e \cdot QE_{PHD} \cdot f \quad (7.2)$$

$f$  is the pulse frequency and  $e$  is the elementary charge.

The number of photons per pulse  $N_{ph}$  can be calculated as follows:

$$N_{ph} = \frac{I_{PHD}}{QE_{PHD} \cdot f \cdot e} \quad (7.3)$$

Figure 7.2 shows the quantum efficiency of the photodiode. For the correct calculation of the number of photons per pulse, the quantum efficiency of the photodiode at the wavelength of the used LED is needed. Figure 7.3 shows the spectrum of one of the used LEDs, it peaks at a wavelength of 471 nm, similar to the multiplication of the Cherenkov spectrum with the water transparency shown in section 4.1. The fact that the spectrum of the used LED is similar to the expected spectrum in the experiment makes the measurement more faithful. The quantum efficiency, the PHD has, when it is illuminated with the LED is calculated as follows:

$$QE_{PHD}(LED) = \frac{\sum_{\lambda} QE_{PHD}(\lambda) \cdot I_{LED}(\lambda)}{\sum_{\lambda} I_{LED}(\lambda)} \quad (7.4)$$

Where  $I_{LED}(\lambda)$  is the normalized intensity of the LED at each wavelength. For the shown LED spectrum the quantum efficiency of the PHD is 68.21 %.

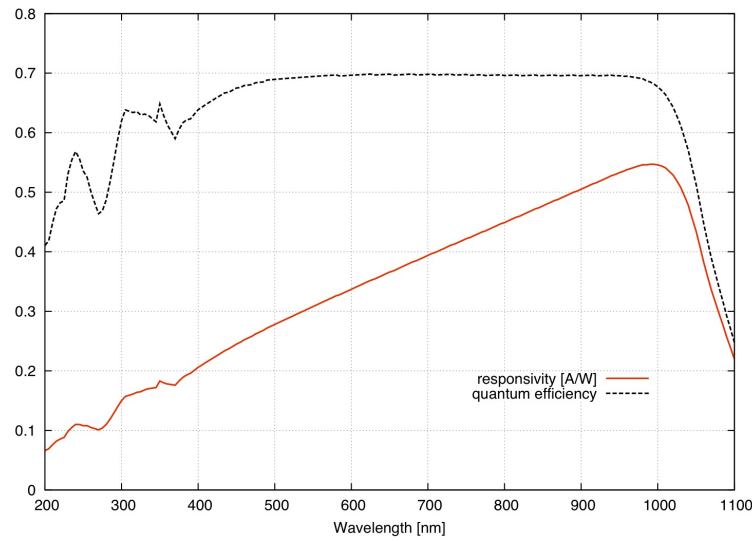


Figure 7.2: Quantum efficiency of the calibrated photodiode Thorlabs SM1PD2A

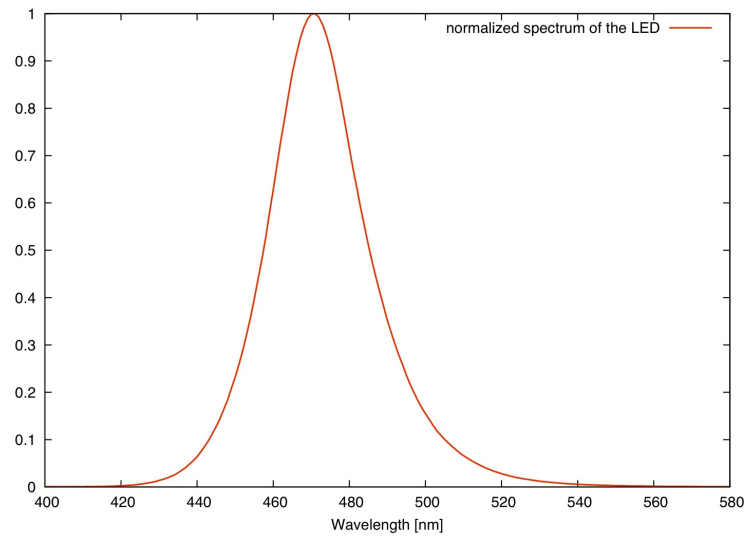


Figure 7.3: Spectrum of one of the used LEDs measured with a monochromator

## 7.2 Design of the test bench

A schematic picture of the test bench is shown in figure 7.4. The test bench is placed in a dark room. In the first measurements the PMT is placed in a carton box with a small opening in direction to the LED. The LED is mounted behind a thin white paper, which acts as a diffuser. The distance between the opening of the box and the light source is roughly 3 m, so that the produced light field should be homogeneous and insusceptible to small changes of the position

of the PMT or the opening of the box. In order to measure the detection efficiency at different positions of the photocathode of the PMT and to get small enough amounts of photons per pulse at the position of the PMT, a diaphragm is placed in the opening of the box in front of the PMT. Another reason for the choice of the diaphragm is that as much intensity as possible is needed at the PHD but not at the PMT because of its amplification. Therefore, a calibration of the diaphragm relatively to the detection area of the photodiode is needed, which will be discussed in section 7.4. As it is not possible to directly measure with the reference photodiode at the same position as the PMT the PHD is mounted on a scanner, which scans the light field of which the intensity should be inverse proportional to the distance squared. The measured current then is extrapolated to the position of the PMT in the black box, while the factor of the diaphragm has to be noticed. Figure 7.4 shows the measurement procedure where first the light field is scanned by taking measurement points each 5 mm in a whole distance of 500 mm. Afterwards, the PHD is driven down and waveforms are taken with the PMT via the oscilloscope. The absolute detection efficiency is calculated similar as shown in section 7.1, but a calibration factor for the ratio between the size of the diaphragm and the size of the detection area of the PHD has to be added. The current is measured with the PHD ( $I_{PHD}$ ) first without and then with the diaphragm in front of it ( $I_{PHD,diaphragm}$ ). The calibration factor is defined as:

$$A = \frac{I_{PHD}}{I_{PHD,diaphragm}} \quad (7.5)$$

The correct equation to calculate the number of photons per pulse behind the diaphragm is:

$$N_{ph} = \frac{I_{PHD}}{QE_{PHD} \cdot f \cdot e \cdot A} \quad (7.6)$$

In addition, the possibility to measure with the PMT at different positions of the photocathode was added by using two different scanners in the black box. One of them is able to do rotational scans, the other one linear scans. This will be discussed in detail later.

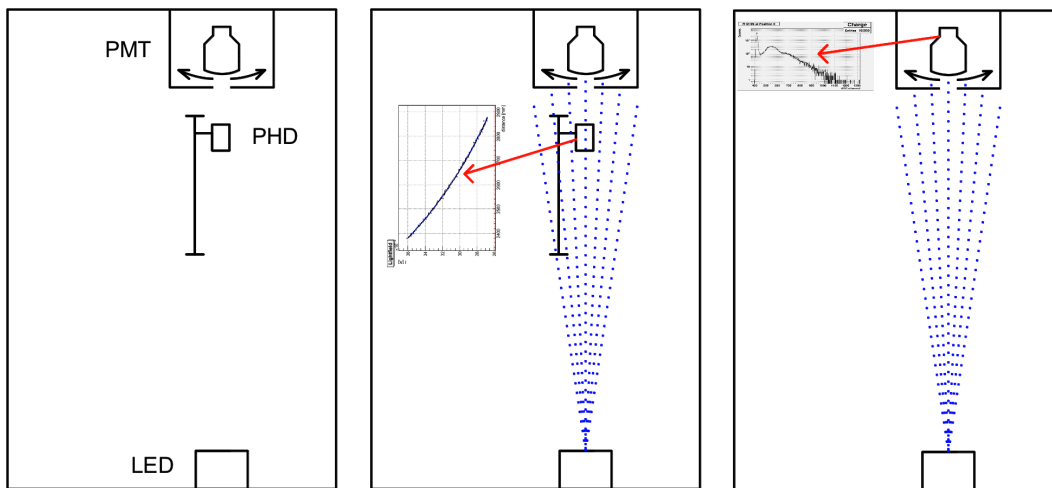


Figure 7.4: Measurement procedure: the PHD first scans the light field , then it is driven down and waveforms are measured with the PMT



## 7.3 Light field

The light field is produced by a LED, which is placed behind a piece of white paper which acts as a diffuser. This will hereinafter be called the light source. The light source is not point like but has a diameter of roughly 5 mm. For the distance of about 2.5 m at the front position of the PHD at the scan and 3 m at the position of the PMT, the light source can be treated as a point source in good approximation. With this requirements, the light field should be inverse proportional to the distance squared. Figure 7.5 shows photos of the light source. As described above it consists of a LED in a box with a diffuser mounted at the front end. To measure the

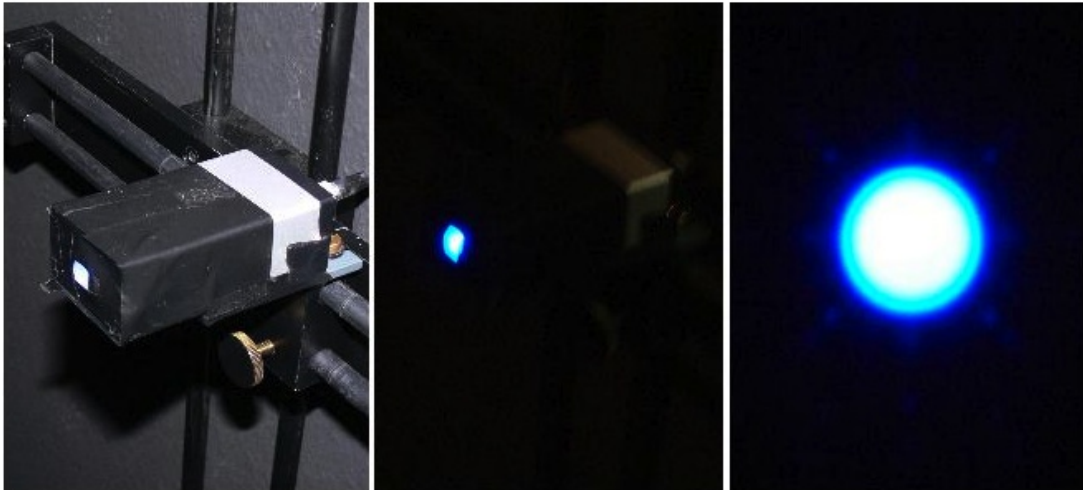


Figure 7.5: Photos of the light source, which consists of a LED in a box and a diffuser at the front end. From left to right: side view of the light source, side view of the light source while switched on, front view of the light source.

light field, a scanner is used, which is equipped with a stepper motor that is driven by a stepper controller. The stepper controller is connected to a PC and is navigated with a self written Python software. The PHD is connected to an amperemeter, which can be read out by the PC and so an automatically executed measurement is possible.

Figure 7.6 shows a light field scan measurement and the expected  $1/x^2$  fit. It is obvious that the measured data points do not follow the  $1/x^2$  fit. An explanation for this behaviour can be found easily by standing in the darkroom while the light source is on. The reflected light from the floor, the walls and especially from the table on which the scanner is mounted can be seen, because it is not black but brown and has a glance surface. The bigger the distance between the light source and the PHD, the bigger is the capability of reflected light from the table reaching the detection area of the PHD. That can be an explanation why the data is flatter than the  $1/x^2$  fit.

To reduce this non controllable systematics, a simple black tube is mounted in front of the PHD and the glance table is covered with black fabric. The black fabric should minimize the reflections of the table and the black tube should keep the residual stray light away from the detection area of the PHD. The black tube is roughly 100 mm long and is lacquered with black mat color. Figure 7.7 shows a measured light field scan with the mentioned improvements. It is obvious, that the Data matches better to the  $1/x^2$  fit. But there are still systematic differences. The differences can result from reflections in the tube itself, because the black lacquer does not

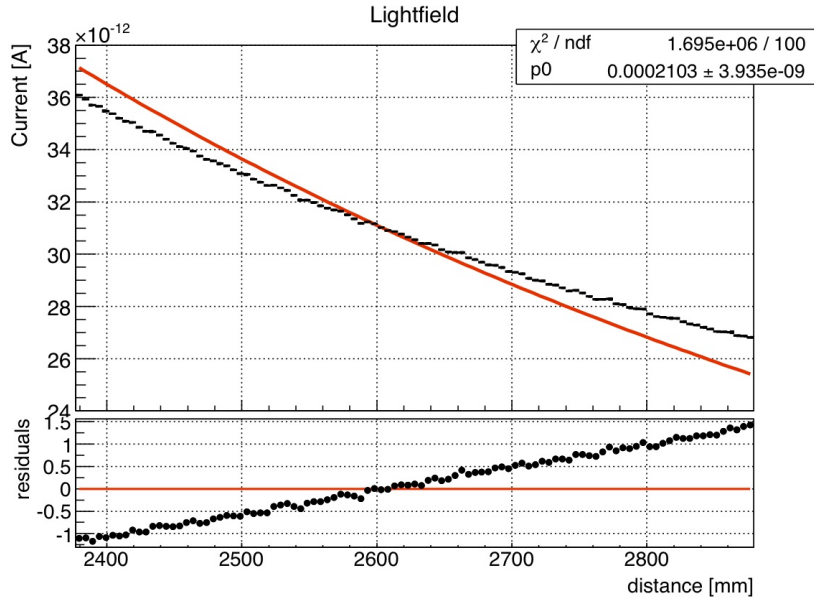


Figure 7.6: Light field scan with a  $1/x^2$  fit. There are big systematic differences.

absorb perfectly. The quality of the fit is calculated as the  $\chi^2$  over the number of degrees of

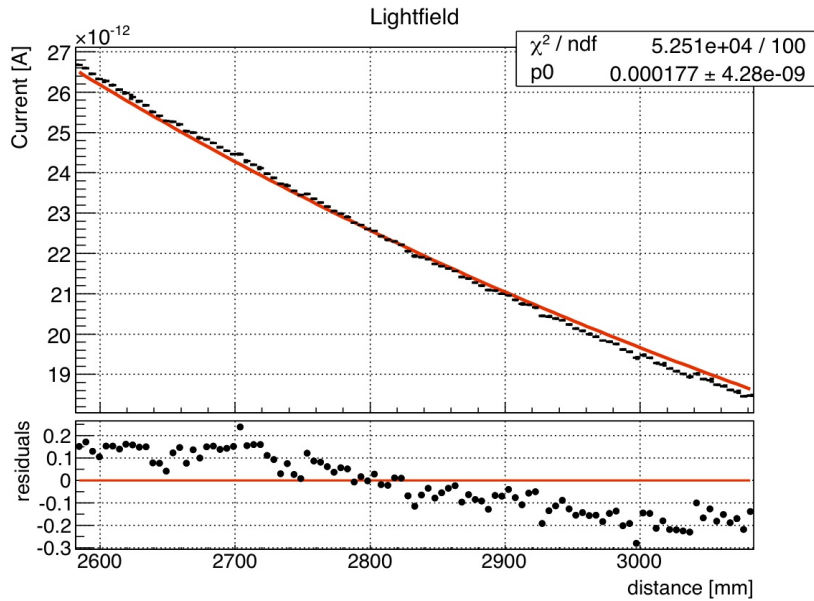


Figure 7.7: Light field scan with mounted black lacquered tube in front of the PHD and the table covered with black fabric.

freedom  $n_{df}$ . For a perfect fit this quotient is equal to 1. The quality of the  $1/x^2$  fit is not very good yet. To improve the fit quality, the light field data is fitted with a  $a/x^b$  function. Figure 7.8 shows the light field with a fit function of  $a/x^b$ . The quality of the fit is much better and the residuals seem to be statistically deviated around zero. The fit quality  $\frac{\chi^2}{n_{df}}$  is still far away from 1, the value of a perfect fit. The main reason for that could be the drift of the picoammeter at low currents, that is bigger than the statistical error. The value of the residuals is of the order

of  $1 \cdot 10^{-13}$  A. It seems realistic, to have a drift in this order of magnitude.

The current at the position of the diaphragm is extrapolated from the data and the number of photons per pulse behind the diaphragm can be calculated. The extrapolated value of the current at the position of the diaphragm (3283 mm) is  $I_{\text{diaphragm}}(3283) = 0.0161$  nA. It is very unsafe to extrapolate a value from the  $1/x^b$  fit, because this shape is not expected. As the differences of the measured and the expected shape probably result from reflected light, it is not sure if the shape of the light field at the position of the PMT is the same as for the fitted region. It is important to eliminate the problem of reflected light, to measure a  $1/x^2$  shape of the light field, so the extrapolation should be safer.

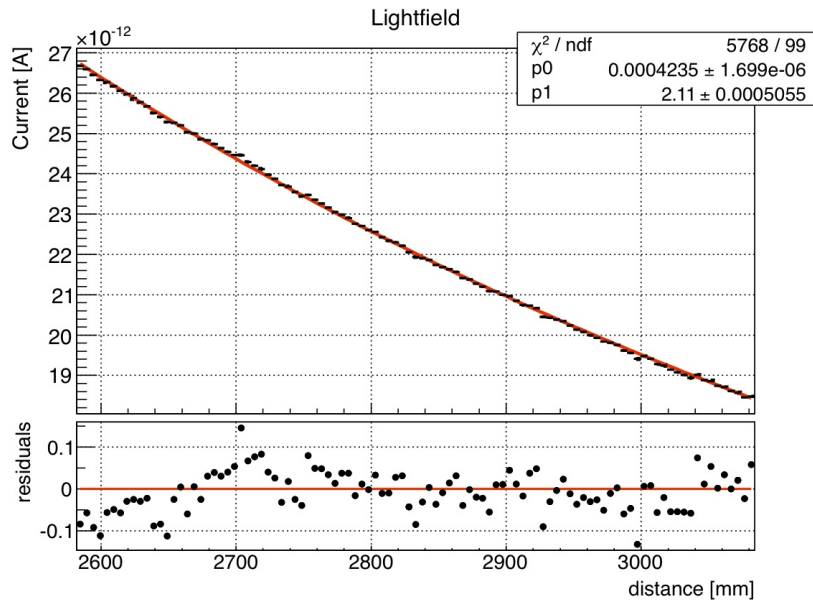


Figure 7.8: Light field scan with a  $a/x^b$  fit to extrapolate the value at the position of the diaphragm.

## 7.4 Calibration of the diaphragms

To calculate the ratio of the number of photons reaching the detection area of the PHD and the photons passing the diaphragm, a current measurement with the diaphragm in front of the PHD is made. Four diaphragms with different diameters ( $\approx 0.85$  mm,  $\approx 1.3$  mm,  $\approx 2.0$  mm and  $\approx 2.8$  mm) were tested. The top picture of figure 7.9 shows the calibration factor  $A$  for the different diaphragms at different distances to the light source. The calibration factor is calculated as follows:

$$A = \frac{\text{measured current without diaphragm}}{\text{measured current with diaphragm}} \quad (7.7)$$

The bottom picture in figure 7.9 shows the normalized calibration factor. Especially for the small diaphragms, the ratio  $A$  is not constant. Furthermore, a trend can be seen, that the ratio increases with the distance. A possible explanation could be, that for the small diaphragms a point source is not a good approximation for the light source at small distances any more. As

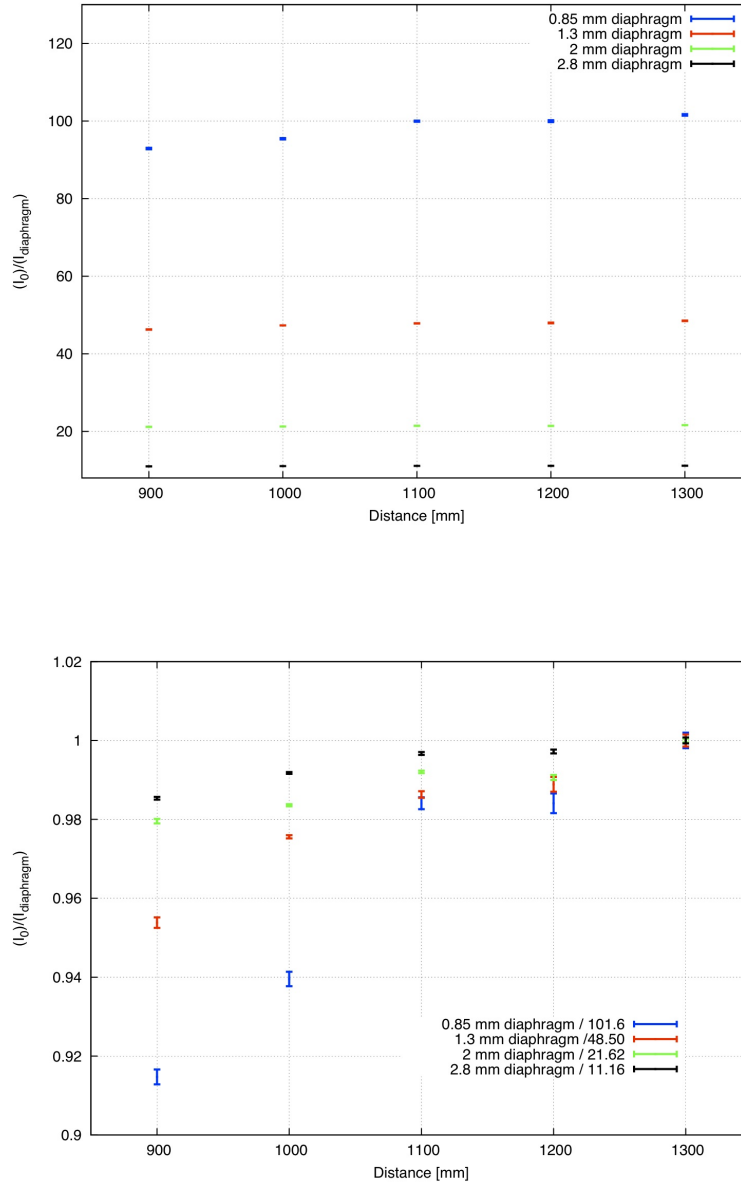


Figure 7.9: Top: the measured calibration factor for the different diaphragms at different distances to the light source. Bottom: the normalized calibration factor, with a trend to be higher for greater distances.

the light field measurement takes place at greater distance and the values for the ratio  $A$  are more or less constant for the greatest distances measured, these values should be the values to take for the calculation of the number of photons passing the respective diaphragm. With these informations, it is now possible to calculate the number of photons per pulse passing the diaphragm. The chosen values for the calibration factor  $A$  are 102, 48.5, 21.6 and 11.2 for the diaphragms with a diameter of  $\approx 0.85$  mm,  $\approx 1.3$  mm,  $\approx 2.0$  mm and 2.8 mm. In this measurement the diaphragm with a diameter of  $\approx 1.3$  mm is used. With this diaphragm, the

single electron spectrum has a mean value of photoelectrons per pulse of lower than 0.5 and so the minimum between the pedestal peak and the single electron peak can be resolved very well. The frequency of the pulses is 2 MHz. The number of photons per pulse is:

$$N_{ph} = \frac{I_{PHD}}{QE_{PHD} \cdot f \cdot e \cdot A_{0,2}} = \frac{0.0161 \cdot 10^{-9} \text{A}}{0.6821 \cdot 2 \cdot 10^6 \text{s}^{-1} \cdot 1.602 \cdot 10^{-19} \text{As} \cdot 48.5} = 1.528 \quad (7.8)$$

## 7.5 Measurement of waveforms with the PMT

To calculate the number of measured photoelectrons per pulse with the PMT, waveforms are recorded with the oscilloscope. The measurement was performed with a PMT of the British company ET Enterprises Ltd. as shown in chapter 6. The waveforms can be saved as binary files in sequences of 500. A C++ code reads these files, calculates the charge below each signal in a given time window and saves every charge value into an ASCII file. The C++ code also displays single events, sum of waveforms to determine the integration window and the emerging histogram of charge. Figure 7.10 shows from top left to bottom right: a single waveform event, the sum of all waveforms and the chosen integration window, an event with high amplitude (threshold:  $-1.4 \text{ V}$ ) and the histogram of charge, consisting of the integration of the signal voltage in the time window for 78000 events. In this measurement, an external amplifier was used, therefore the peak voltage of the signals is relatively high.

The high amplitude window in figure 7.10 shows a strange event with really high voltage and

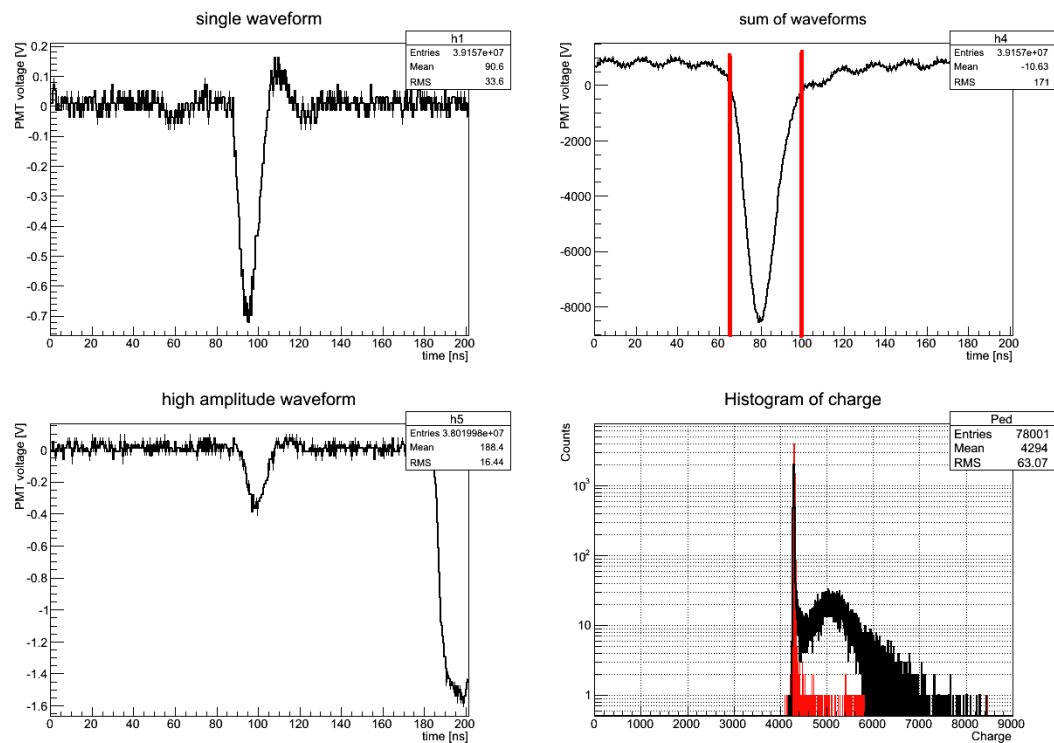


Figure 7.10: Top left to bottom right: a signal from the light source, the sum of all waveforms and the integration window, a high amplitude event and the histogram of charge.

a broad signal additionally to a normal event. This big and late event could be an afterpulse as

described in section 5.4, that not necessarily results from the signal shown in the same window. As the frequency of the pulses is 2 MHz, this afterpulse can result from a pulse that was measured even before. A characteristic time delay for afterpulses is 100 ns to 1  $\mu$ s. Such events are excluded by the determination of the integration window.

There are two ways to determine the measured number of photoelectrons per pulse with the histogram of charge. The one way is shown in figure 7.11. The number of electrons in the histogram is fitted with a poisson distribution. Each n-electron peak and the pedestal have a gaussian shape. It is also possible to fit the exponential noise. A detailed description of the fit mechanism can be found in [12]. The fit shown in figure 7.11 is modified in this way, that the events of the single electron peak below the pedestal are taken into account. The method in [12] does not take these values into account. The assumption is that the error of counting the values of the single electron peak below the pedestal, that are obviously not measured is smaller than removing events by making a cut at the mean of the pedestal.

The number of pedestal and non pedestal events is calculated via the fit functions. The other way to determine the number of measured photoelectrons per pulse, is to choose a threshold in the minimum between the pedestal peak and the single photoelectron peak (see figure 7.12). All electrons with lower charge than the threshold are characterised as zero events ( $n_{ped}$ ). The events with higher charge are at least single electron events and thus regarded as a signal. The number of photoelectrons per pulse ( $\lambda$ ) is calculated as described in section 5.4:

$$\lambda = -\ln \frac{n_{ped}}{n_{all}} \quad (7.9)$$

If the threshold method is used, it is nevertheless necessary to do the fit, to check if the number of electrons in the histogram is really poisson distributed.

In figure 7.11 the exponential fit can clearly be seen, as the right slope of the pedestal gauss flattens before the minimum is reached. Single, double and triple electron events can be identified by the fit. Even though the single electron gauss fit to the left ranges below the pedestal, which is definitely a wrong assumption, the fit quality is very good with  $\chi^2 \approx 1.01$ , so the number of electrons in the histogram is really poisson distributed. The calculated number of measured photoelectrons per pulse is 0.2938.

In figure 7.12 the threshold is set to ADC channel 898 which is identified as the minimum between the pedestal and the single electron peak. The measured number of photoelectrons per pulse here is 0.2994. The relative difference for the two different methods is roughly 2 %.

## 7.6 Calculation of the detection efficiency

Now that the number of photons per pulse and the number of measured photoelectrons per pulse are known, the absolute detection efficiency of the PMT can be calculated:

$$DE = \frac{\text{photoelectrons per pulse}}{\text{photons per pulse}} = \begin{cases} \frac{0.2938}{1.528} = 0.1923 & \text{gauss fit method} \\ \frac{0.2994}{1.528} = 0.1959 & \text{threshold method} \end{cases} \quad (7.10)$$

For the shown measurement, the diaphragm and so the light spot was positioned in the middle of the photocathode of the PMT (ETEL D783KFLA). In addition to this measurement, a rotational scan is made, waveforms are measured and the detection efficiency is calculated the same

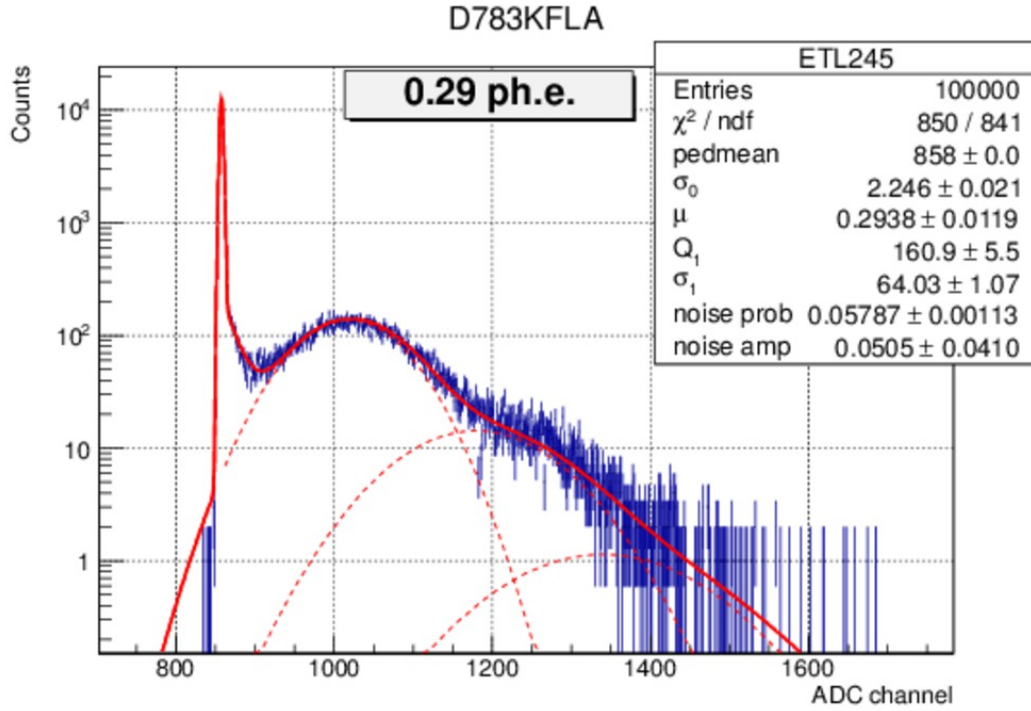


Figure 7.11: Histogram of charge from a measurement with the ETEL D783KFLA PMT and the fit with exponential noise. The number of measured photoelectrons per pulse is 0.2938.

way as above. The rotational radius (14.1 cm) can not be adapted to be equal to the radius of curvature of the front window of the PMT (19.8 cm), because the position of the diaphragm is fixed relatively to the center of rotation and so the rotation radius can not be adjusted at will. So the position of incidence of the light at the photocathode is calculated from the angle information. Table 7.1 shows the measured number of photoelectrons and the calculated detection efficiency for different positions of the light spots on the photocathode. As the zero position of the measurement was not exactly in the center of the photocathode, the position was corrected and shifted a few mm. The errors shown in table 7.1 are calculated with the gaussian error propagation of the equation:

$$DE = \frac{N_{pe}}{N_{ph}} = \frac{N_{pe} \cdot QE_{PHD} \cdot f \cdot e \cdot A_{0,2}}{I_{PHD}} \quad (7.11)$$

The known statistical errors of  $N_{pe}$  and  $I_{PHD}$  were used to calculate the statistical error:

$$\Delta DE = DE \cdot \sqrt{\left(\frac{\Delta N_{pe}}{N_{pe}}\right)^2 + \left(\frac{\Delta I_{PHD}}{I_{PHD}}\right)^2} \quad (7.12)$$

Figure 7.13 shows the detection efficiency and the statistical error for the different positions at the photocathode (ET D783KFLA). As the radius of rotation is not equal to the radius of curvature of the PMT window, the angle of incidence for the off-center position is not  $90^\circ$ . Therefore, the detection efficiency should fall at larger distances from the center, because of larger reflections at the glass. At the edges of the PMT front window, the detection efficiency is significantly



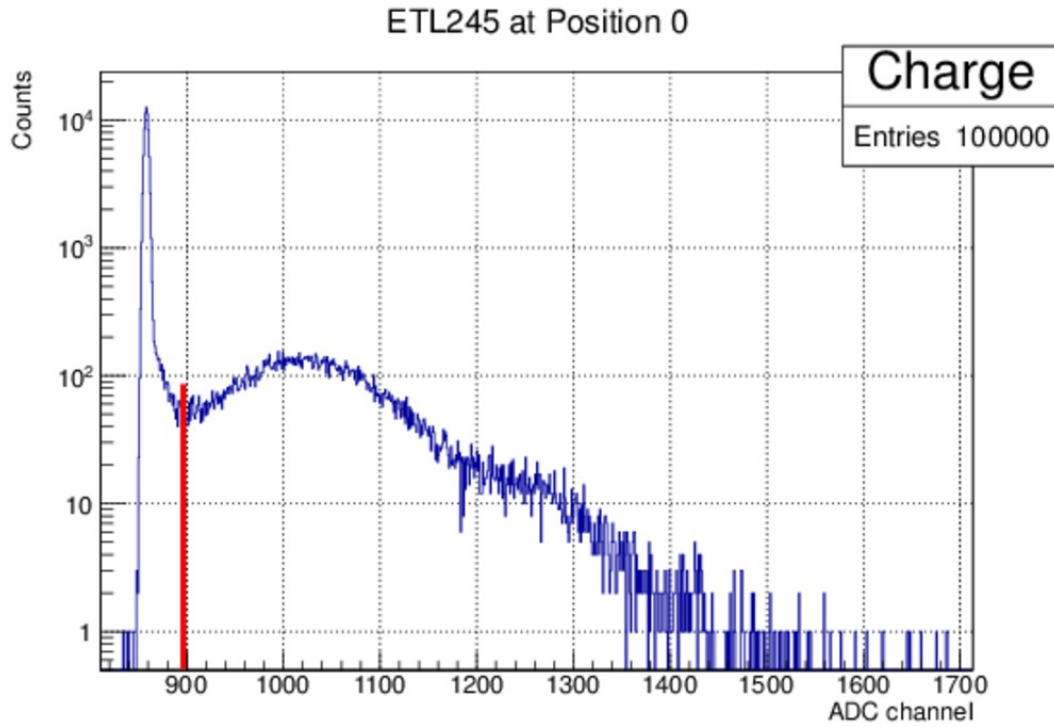


Figure 7.12: Same histogram of charge as in figure 7.11 and the threshold described above.

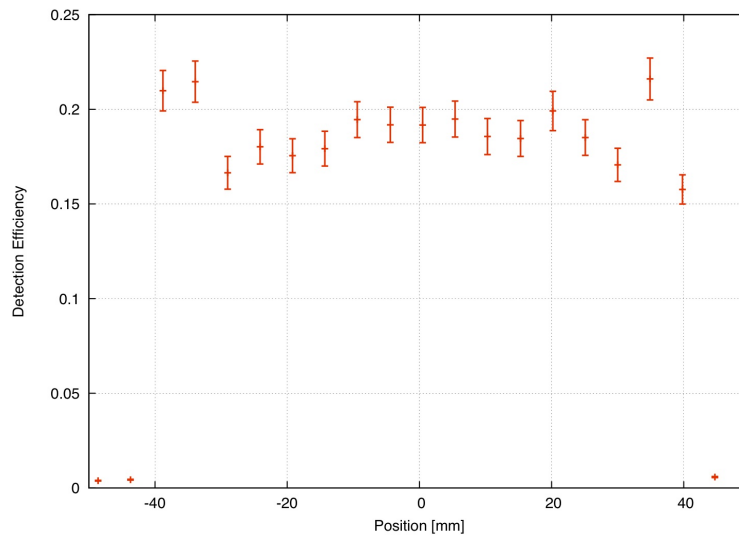


Figure 7.13: Detection efficiency with errors for different positions on the photocathode (ETEL D783KFLA).

higher than in the center. That can be explained by the reflective area shown in figure 8.2. Photons that pass the photocathode without producing a photoelectron can be reflected at this area



Position [mm]	$N_{pe}$ (multi gauss fit)	$DE$	$\Delta_{stat} DE$	$\frac{\Delta_{stat} DE}{DE} \cdot 100$
-53.5	0.0050	0.00326	0.00016	4.8
-48.6	0.0059	0.00385	0.00019	4.8
-43.7	0.0067	0.00437	0.00021	4.8
-38.8	0.3214	0.210	0.011	5.1
-33.9	0.3287	0.215	0.011	5.1
-29.0	0.2550	0.1665	0.0087	5.2
-24.1	0.2760	0.1802	0.0091	5.1
-19.2	0.2688	0.1755	0.0090	5.1
-14.3	0.2745	0.1792	0.0092	5.1
-9.4	0.2980	0.1945	0.0095	4.9
-4.4	0.2938	0.1918	0.0093	4.9
-0.5	0.2936	0.1917	0.0093	4.9
5.4	0.2984	0.1948	0.0095	4.9
10.3	0.2843	0.1856	0.0095	5.1
15.3	0.2827	0.1846	0.0095	5.1
20.2	0.3050	0.199	0.010	5.2
25.1	0.2835	0.1851	0.0094	5.1
30.3	0.2614	0.1707	0.0088	5.1
34.9	0.3309	0.216	0.011	5.1
39.8	0.2415	0.1577	0.0077	4.9
44.7	0.0088	0.00575	0.00028	4.8

Table 7.1: Values of the number of photoelectrons, the detection efficiency and the statistical error of the detection efficiency (ETEL D783KFLA).

and hit the photocathode again. Furthermore, photons can produce electrons at the reflecting areas, as they are also covered with photocathode material. The overall probability to produce a photoelectron and so the detection efficiency rises.

## 7.7 Measurement with the Hamamatsu PMT

Another measurement is made with a new Hamamatsu R12199 PMT. It is another candidate for the KM3NeT project and is designed for the special requirements. The PMT surface was scanned the same way as shown in section 7.6. The radius of curvature of the front window of the PMT (5 cm) is much smaller than the radius of rotation (here 16.2 cm), so the effect of non perpendicular incidence of light is stronger than for the measurement with the ETEL PMT. For the light field scan, the lacquered tube in front of the PHD was covered with better absorbing material, which should suppress the reflections in the lacquered tube. It is obvious, that the light field, shown in figure 7.14 follows the  $1/x^2$  law much better than without the absorbing material in the tube, as for the measurement with the ETEL PMT. The main part of the reflections seems to be suppressed. The value of the residuals is again of the order of  $1 \cdot 10^{-13}$  A, nevertheless the reduced  $\chi^2$  value is much smaller as for the light field scan without the absorbing mate-

rial in the tube. This strengthens the assumption that the residuals mainly result from the drift of the picoamperemeter. As mentioned in section 7.6, the extrapolation should be safer for a light field with a  $1/x^2$  shape. The histogram of charge, shown in figure 7.15 has a very broad

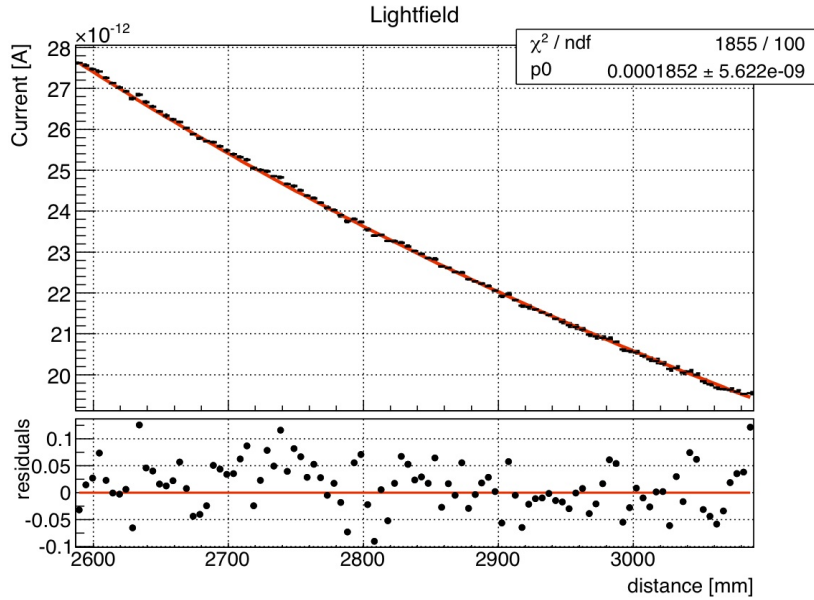


Figure 7.14: Light field scan with the tube, covered with absorbing material. A  $a/x^2$  function was fitted.

pedestal. This can be identified as a shifting of the pedestal level during the measurement, due to electronic noise. To avoid this broadening, the C++code is modified in the way, that for every waveform the level of pedestal is integrated before the time window for the integration of the signal. The integrated pedestal then is subtracted from the integrated signal, so that the broadening disappears, because the shift of the pedestal level is eliminated. The modified histogram of charge is shown in figure 7.16. It is made with the same raw data as the broad histogram.

Table 7.2 shows the values for the position at the photocathode, the number of measured photoelectrons per pulse for the threshold and the multi gauss fit method, the calculated detection efficiency for both methods and the statistical errors of the detection efficiency, calculated the same way as in section 7.6. In two cases, the errors from the fit method are very small, because the fit program sometimes delivers too small errors for the number of photoelectrons for non clear reason. The errors from the threshold method should be more credible. Figure 7.17 shows the plotted detection efficiency for both methods. Hereinafter it will be very important to have a  $1/x^2$  dependent light field, to get a safer extrapolation. Furthermore it is important to have two equal tubes, that the calibration of the diaphragm is made under the same conditions as the measurement, both with tubes in front, to have the  $1/x^2$  dependency and as less reflected light as possible.

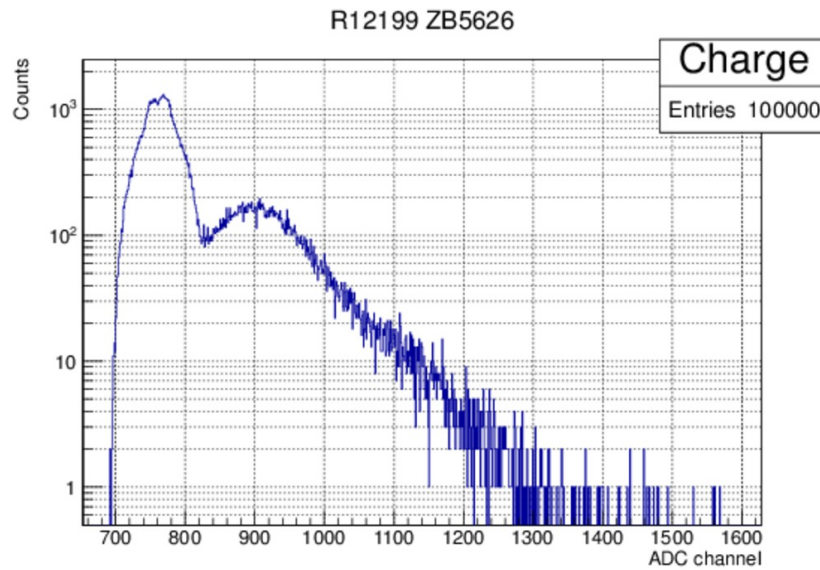


Figure 7.15: Histogram of charge with the broad pedestal due to the shifting of the pedestal level.

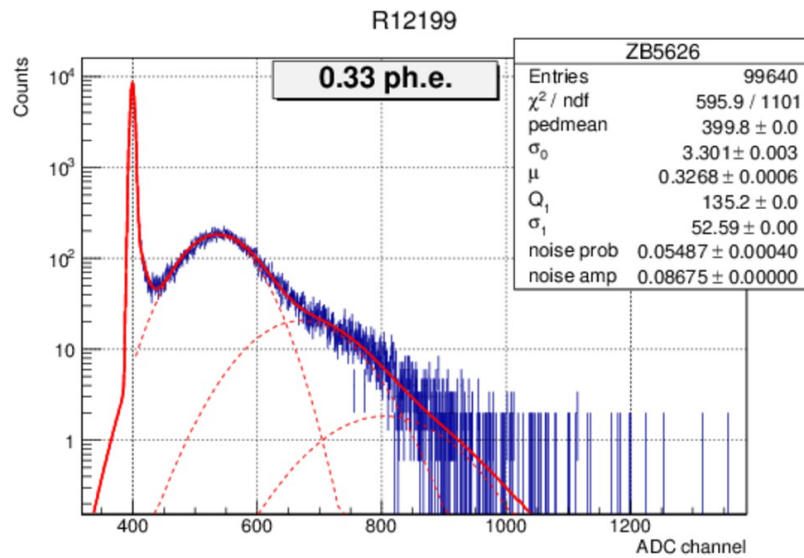


Figure 7.16: Modified histogram of charge with a much smaller pedestal, because of the event per event correction.

Position [mm]	DE (multi gauss)	$\frac{\Delta_{stat} DE}{DE} \cdot 100$	DE (threshold)	$\frac{\Delta_{stat} DE}{DE} \cdot 100$
-44.5	$1.214 \cdot 10^{-6}$	0.080	0.00346	55
-34.4	0.1839	0.86	0.1904	1.2
-22.1	0.1938	1.2	0.2027	1.1
-8.5	0.2002	0.08	0.2016	1.1
5.6	0.1970	0.44	0.1974	1.1
5.6	0.1987	0.10	0.1993	1.1
19.4	0.2044	0.84	0.2088	1.1
32.1	0.1802	0.91	0.1845	1.2
42.7	0.00291	10	0.00358	54

Table 7.2: Values of the detection efficiency and the relative statistical error for the multi gauss fit and the threshold method (Hamamatsu R12199).

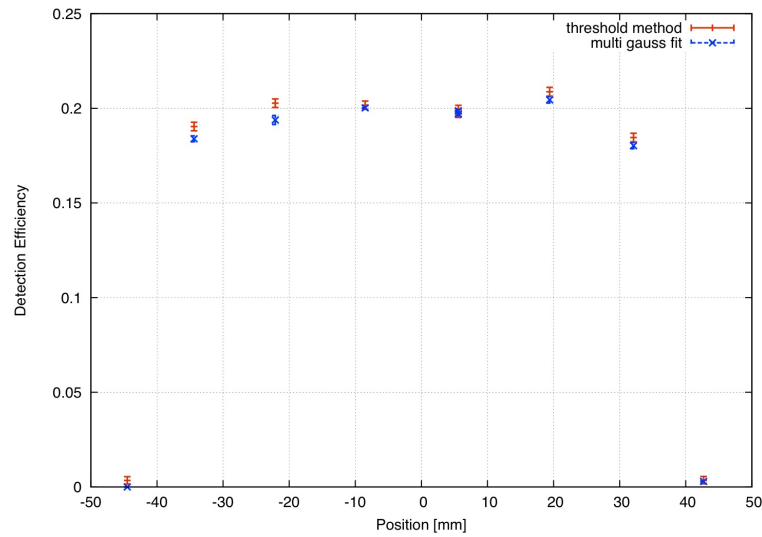


Figure 7.17: Detection efficiency for the Hamamatsu R12199 PMT with both, the multi gauss fit and the threshold method.

# Chapter 8

## Quantum efficiency measurement

In this chapter, quantum efficiency measurements with the ETEL and the Hamamatsu PMT are shown. Linear scans of the photocathode, as shown in figure 8.2 are also performed and the collection efficiency near the center position of the photocathode is calculated.

### 8.1 Measurement principle

The quantum efficiency of a PMT photocathode is measured during its dynode system is shorted with the anode. The PMT is illuminated with a constant light source and the current is measured at the anode ( $I_{PMT}$ ) while the photocathode has negative potential. The photoelectrons, produced by the photons, are accelerated towards the dynode-anode-system and can be measured as a current. As a reference, the current is measured with a PHD ( $I_{PHD}$ ) with known quantum efficiency  $QE_{PHD}$  under the same conditions. The quantum efficiency of the PMT can be calculated as follows:

$$QE_{PMT} = QE_{PHD} \cdot \frac{I_{PHD}}{I_{PMT}} \quad (8.1)$$

### 8.2 Quantum efficiency scan

As a light source, a xenon lamp is used for the quantum efficiency scan. The spectrum of the lamp is shown in figure 8.1. The light is directed to a monochromator, which can adjust any wavelength between 200 and 1000 nm. As the maximum of the spectrum of the LED, used for the detection efficiency measurement, is at roughly 470 nm, this wavelength is also used for the quantum efficiency measurement.

The scan is performed by the same scanner, that is used for the light field measurement, but it's not a rotational scan, as for the detection efficiency, but a linear scan. Figure 8.2 shows the configuration of the different scans. The top left picture shows the different light beam positions and directions for the linear scan. The top right picture shows a possible trace of a photon, that does not produce a photoelectron at the first hit of the photocathode. This photon can then produce an electron at the reflecting material, because this material is also covered with photocathode material from the vapor deposition. If the photon doesn't produce an electron, it can be reflected again etc. It can finally come back to the photocathode and produce an electron. The bottom picture shows the light beam position and direction with rotational scans for not necessary equal radius of rotation and radius of curvature of the PMT front window. The

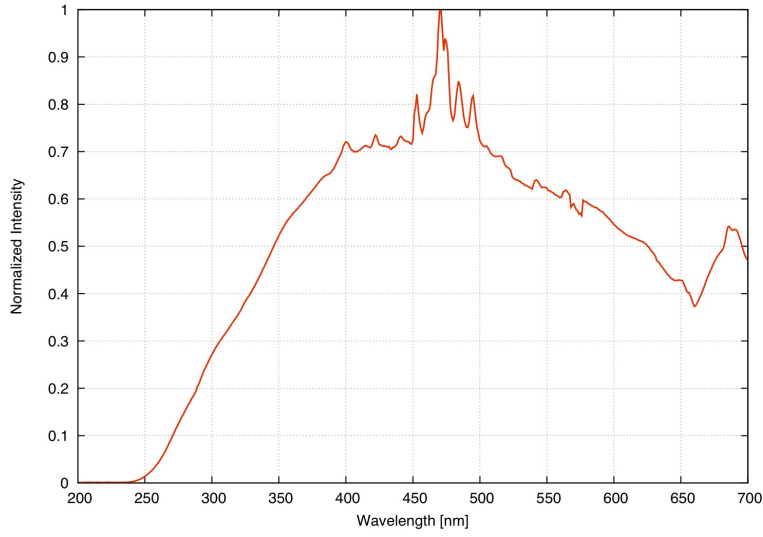


Figure 8.1: Normalized spectrum of the used xenon lamp.

reflecting material is not hit by the photons during a rotational scan. At a detection efficiency measurement, the effect of photo electron production at the reflecting area should not influence the results very much, because the equipotential lines of the electric field in the PMT avoid, that electrons near these reflecting material can be guided to the first dynode. At a quantum efficiency measurement, when everything but the photocathode is on the same potential, these photoelectrons at the reflecting areas contribute to the measured current and so to the quantum efficiency.

Figure 8.3 shows the quantum efficiency scan (linear) and the detection efficiency scan (rotational) for the ETEL PMT. It is obvious, that the reflections strongly influence the result of the measurement, because at the positions, where the reflecting material is in the direction of the light beam, a peak of the quantum efficiency emerges. The peak of the quantum efficiency is located at roughly  $\pm 30$  mm. The collection efficiency ( $CE$ ) near the center is calculated by the following equation:

$$CE = \frac{DE}{QE} = \frac{0.1917}{0.1944} = 0.9861 \quad (8.2)$$

The collection efficiency near the center is almost 100 %. For positions near the edges of the front window it is not possible to determine the collection efficiency, because of the reflections due to the different types of scans. To get the collection efficiency as a function of the position, rotational scans or linear scans for both, the detection efficiency measurement and the quantum efficiency measurement have to be done.

Figure 8.4 shows the quantum efficiency scan and the detection efficiency scan for the Hamamatsu PMT. Similar to the ETEL measurement, the peaks of the quantum efficiency are located at  $\pm 30$  mm. The collection efficiency near the center (at  $-8.5$  mm) is:

$$CE = \frac{DE}{QE} \approx \frac{0.2016}{0.2178} = 0.9256 \quad (8.3)$$

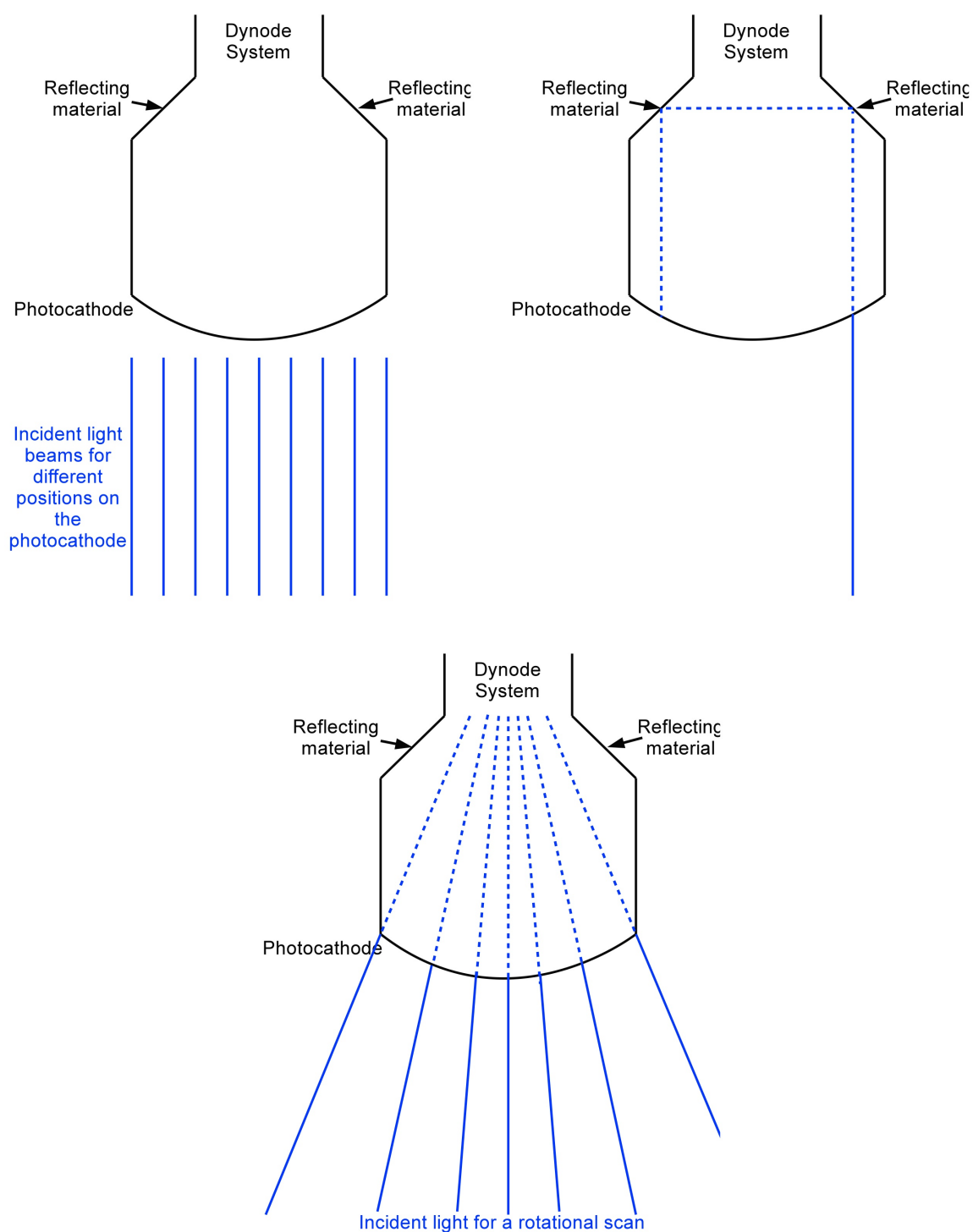


Figure 8.2: The figure emphasizes the principle of the scans with the PMT. The top left picture shows a linear scan and how the light hits the photocathode for different positions, the top right picture shows how in this configuration reflections can occur and the bottom picture shows the light traces for a rotational scan.

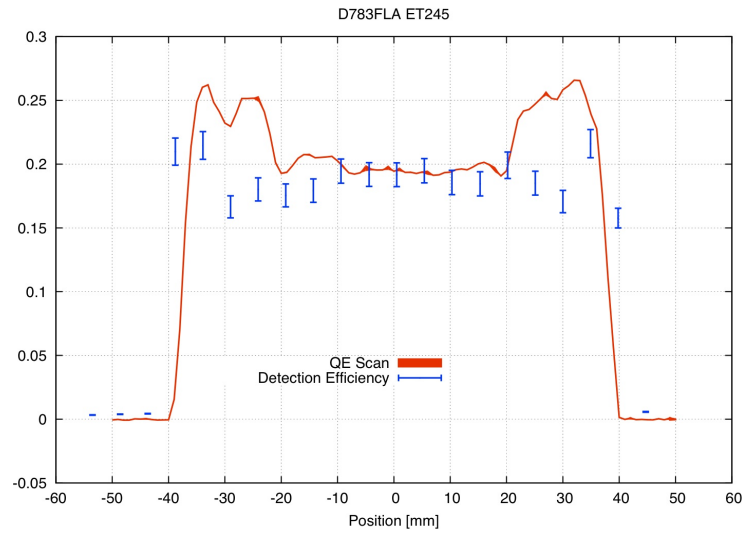


Figure 8.3: Measured detection efficiency with a rotational scan (blue dots) and the quantum efficiency (red line) for the ET245 PMT. The centre of the peak of the quantum efficiency is located at roughly  $\pm 30$  mm.

The collection efficiency of the Hamamatsu PMT is clearly lower than the collection efficiency of the ET245 PMT but still very good. The reflected light, measured with the PMTs for both measurements, still influences the measurement results of the detection efficiency and the collection efficiency, because it is no tube mounted in front of the PMTs, as in front of the PHD. But as a diaphragm is used, of which the diameter is much smaller than of the detection area of the PHD, the influence of the reflected light should not be as strong as for the light field measurement. To remove this systematic effect, equal tubes will be needed in front of the PHD and in front of the diaphragm in the following.



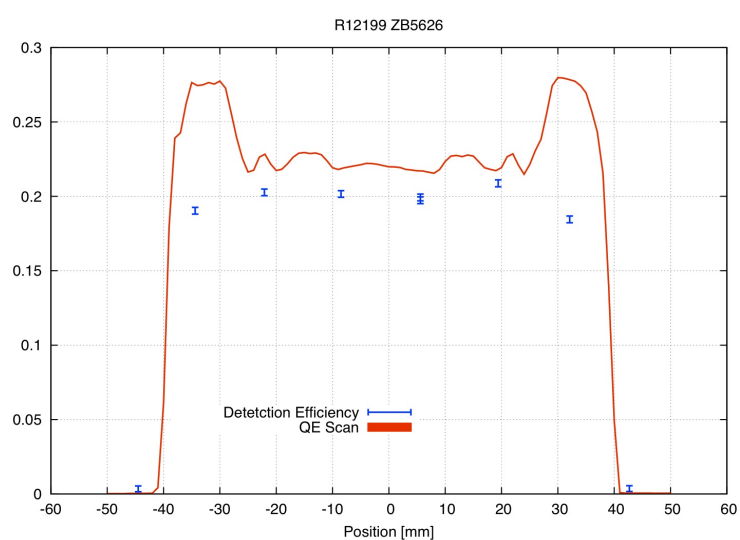


Figure 8.4: Measured detection efficiency with a rotational scan (blue dots) and the quantum efficiency (red line) for the Hamamatsu R12199 PMT. The peak of the quantum efficiency at roughly  $\pm 30$  mm can be explained by the electron production and the reflections at the reflecting material.



# Chapter 9

## Improvement of the test bench

This chapter deals with the improvement of the provisional test bench.

### 9.1 Protective tube

As previous measurements, described in chapter 7.3, reveal a presence of undesired reflected or scattered light inside of the tube, a concept of an improved, protective tube is discussed in this section. The idea is to build two equal tubes to put them in front of the PHD and in front of the PMT to prevent the anywhere reflected or scattered light to reach the detection areas. As reflections do not only occur outside but also inside of the tube, a system of diaphragms inside of the tube can help to suppress the reflected light. The tube has a cylindrical shape with conical diaphragms inside. Figure 9.1 shows a sketch of the layout of the tube.

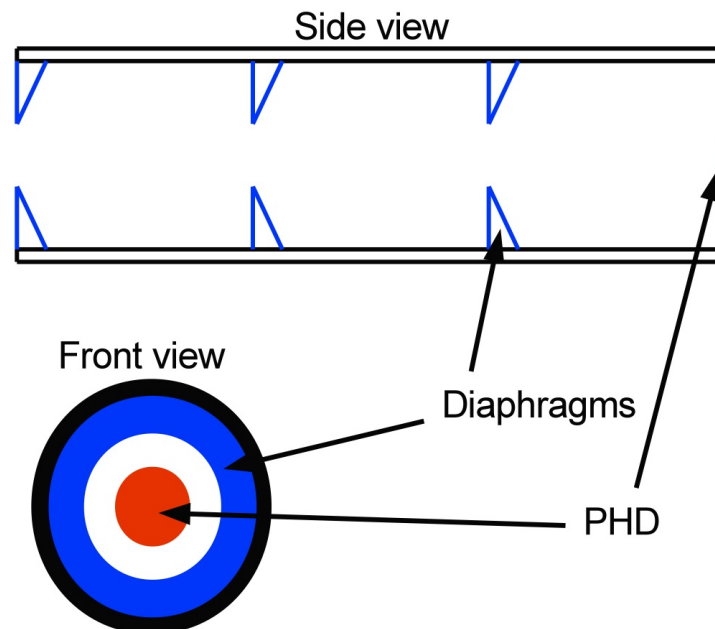


Figure 9.1: Sketch of the tube layout, the diaphragms in blue and the detection area of the PHD in red.

### 9.1.1 Tube simulation

Before the tubes were entered into contract, a simple simulation was made to investigate the effects of the diaphragms. Therefore, a 2D simulation of a cut through the tube was written in Python. A photon is produced at the entrance of the tube with a random position and random angle. The trace of the photon is simulated taking reflections at the diaphragms and the tube itself into account, where the angle of incidence is always equal to the reflection angle. In addition, an absorption coefficient can be adjusted and the position of the diaphragms can be changed. The trace of a photon is calculated every tenth mm. The aim is to find the best position of the diaphragms to block the most reflected photons and to build the tube after this model. Besides reflections, scattering is also possible but is not taken into account in the simulations. Furthermore, 3D results can differ a from the 2D results.

The inner diameter of the tube (26 mm) is determined by the outer diameter of the housing of the PHD, that then can be mounted directly, e.g be screwed into the tube. The diameter of the detection area of the PHD is 9 mm. This area (red in figure 9.1) has to be smaller than the opening area of the diaphragm (white in figure 9.1), to avoid a blocking of not reflected light. Figure 9.2 shows simulations of the tube without diaphragms. The blue dots describe the trace of the photons, the red area is the detection area of the PHD. The inner diameter of the tube is 26 mm, the total length of the tube is 200 mm and the detection area of the PHD has a diameter of 9 mm. The four simulations were executed with 200 events each, the absorption probability was changed from 0.2 top left via 0.5 top right, 0.7 bottom left and 0.9 bottom right. The top

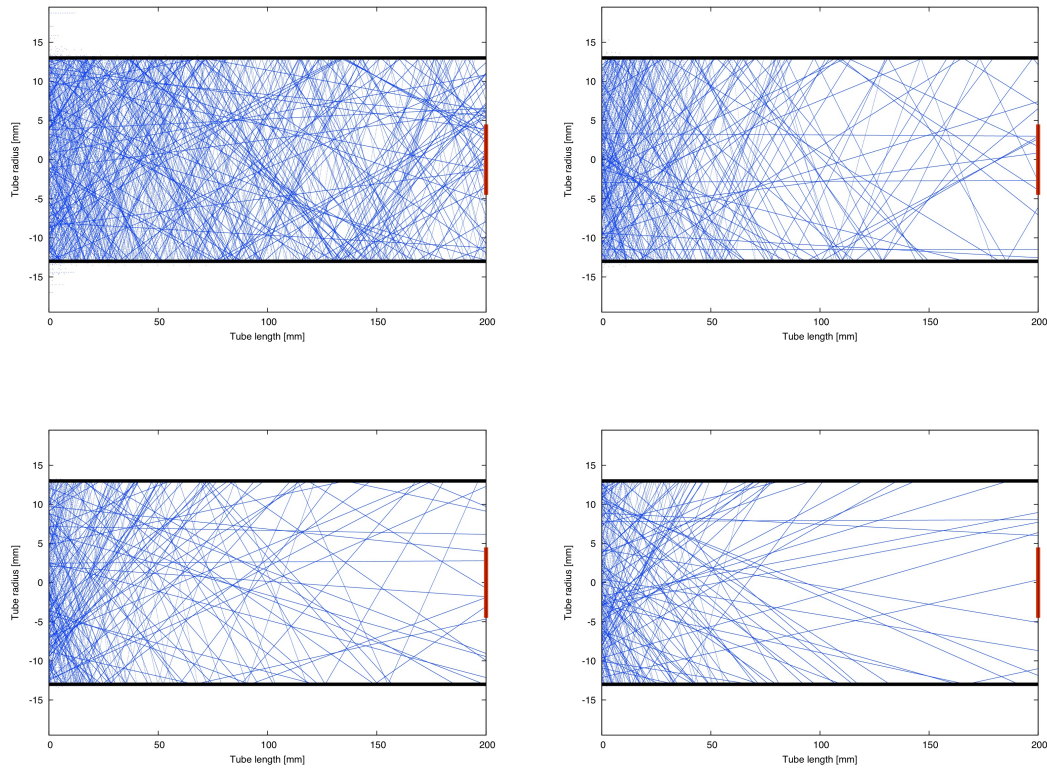


Figure 9.2: Simulations with 200 events each for different absorption probabilities: top left 0.2, top right 0.5, bottom left 0.7 and bottom right 0.9.

picture in figure 9.3 shows only the events which hit the detection area of the PHD for 1000 starting events. There are many not reflected events which hit the PHD. These non reflected events come directly from the light source and do not have to be blocked by the diaphragms. In the following, the simulated events have a minimum angle, so that only reflected events are taken into account. The simulation with a minimum angle of  $3^\circ$  is shown in the bottom picture of figure 9.3. 100 simulations with  $n = 1 \cdot 10^5$  events, the minimum angle of  $3^\circ$ , without

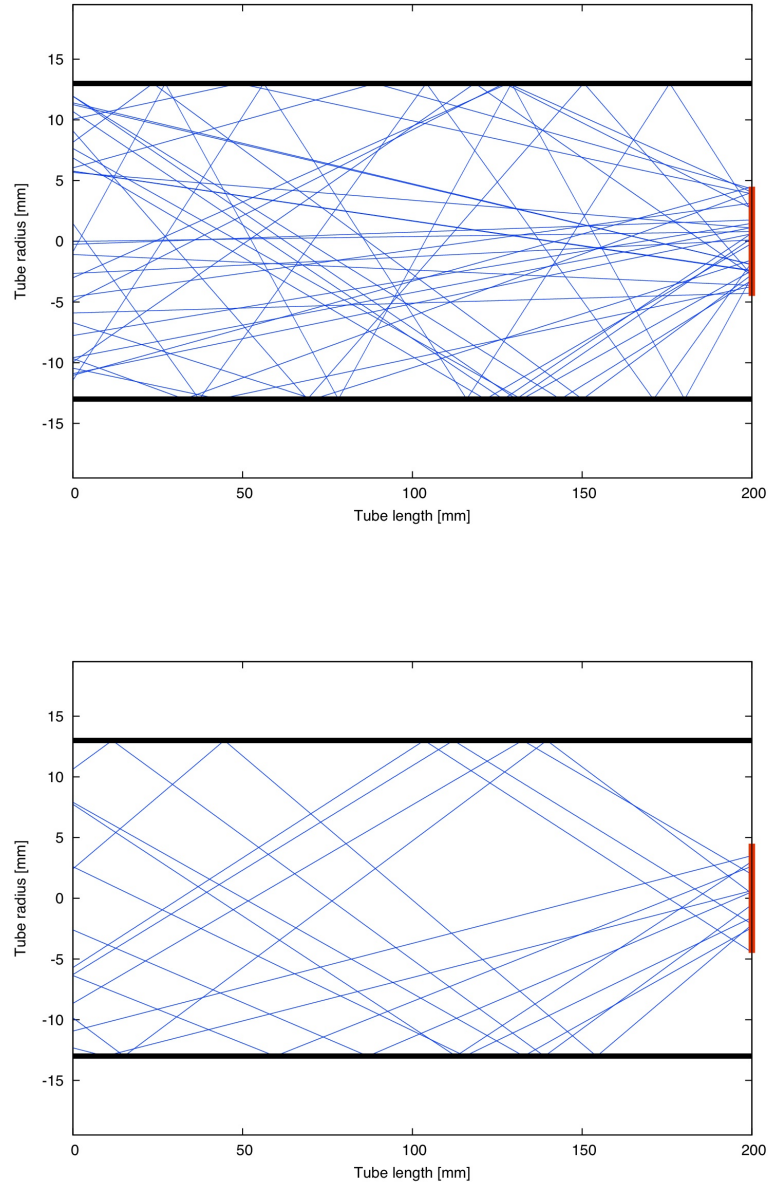


Figure 9.3: Top: only events which hit the PHD. Bottom: only reflected events which hit the PHD.

diaphragms and an absorption probability of 0.7 show that the mean value of events that hit the PHD is  $n_{hit,mean} = 1467$  per simulation with a statistical error of  $\Delta n_{hit,mean} = 3.7$ . Figure 9.4

shows, that the  $n_{hit}$  values are gaussian distributed, following the Central Limit Theorem for random variables and thus it is assumed that the error of the sum of the hitting events off all 100 simulations is  $\Delta n_{hit,sum} = \sqrt{n_{hit,sum}}$ . For the 100 simulations, the sum of all hitting events and the

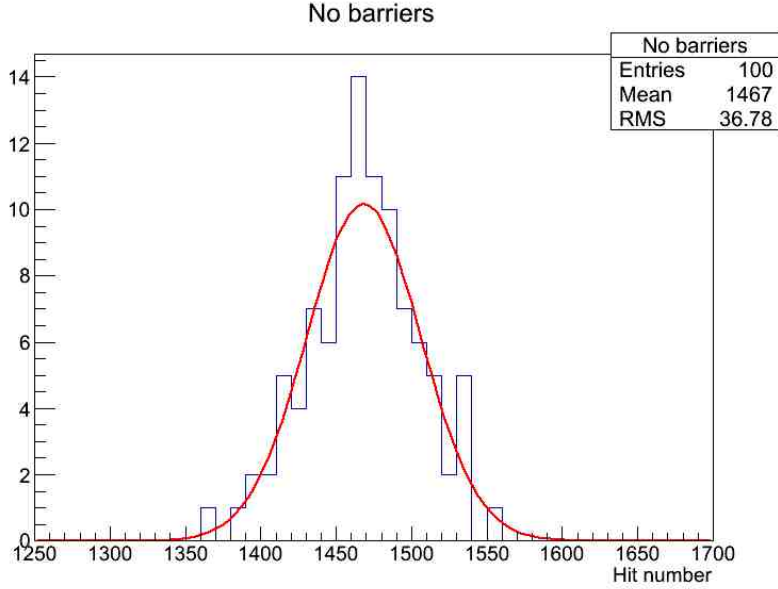


Figure 9.4: Distribution of the hit number of the single simulations with an event number of  $1 \cdot 10^5$  and a gauss fit.

error are:

$$n_{hit,sum} = 146715 \quad , \quad \Delta n_{hit,sum} = \sqrt{n_{hit,sum}} = 383 \quad (9.1)$$

The relative errors for the mean value of the single simulations is nearly equal to the relative error of the sum of all simulations. The relative number of photons that hit the PHD is:

$$n_{rel} = \frac{146715 \pm 383}{1 \cdot 10^7} = (1.467 \pm 0.004)\% \quad (9.2)$$

Now the diaphragms are included in the program code. They are simulated as lines at different positions in the tube with a length of 5 mm each. Figure 9.5 shows a simulation of 200 events with included diaphragms. The diaphragms are positioned at 50, 100 and 150 mm and have a length of 5 mm each. The minimum angle is  $3^\circ$  and the absorption probability is 0.7. No photon hits the PHD. The diaphragm system shields the reflected photons very well. 100 simulations with  $n = 1 \cdot 10^5$  events each are also performed for the configuration with the 5 mm diaphragms at positions of 50, 100 and 150 mm. The mean value of the events, that hit the PHD, is 227 and the statistical error is  $\Delta n_{hit,mean} = 1.6$ . The sum for all 100 simulations and the error are:

$$n_{hit,sum} = 22723 \quad , \quad \Delta n_{hit,sum} = \sqrt{n_{hit,sum}} = 151 \quad (9.3)$$

The relative errors of the events for the single simulations and for the sum of the simulations are again nearly the same. The reduction factor  $r$ , which is the ratio between the number of events hitting the area of the PHD for the simulation with diaphragms at positions 50, 100 and 150 mm and for the simulation without diaphragms is:

$$r = \frac{22723}{146715} = 0.155 \quad (9.4)$$

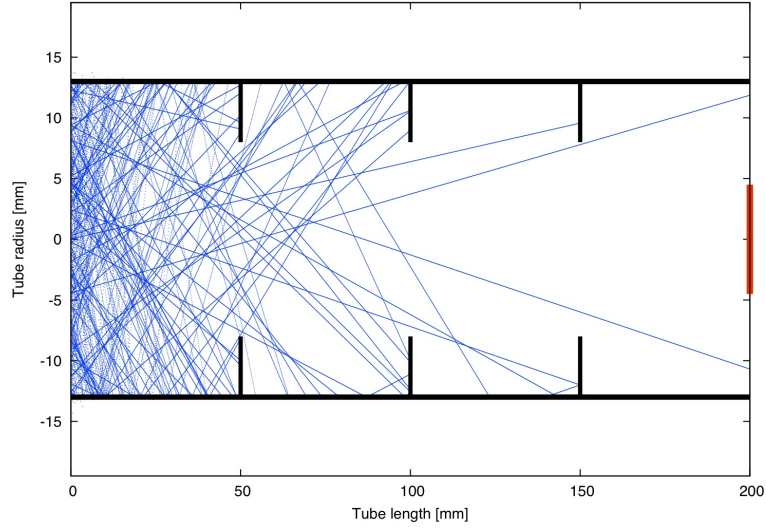


Figure 9.5: 200 events with diaphragms at 50, 100 and 150 mm. All diaphragms have a length of 5 mm. The photons are shielded very well and no photon hits the PHD. A minimum angle of  $3^\circ$  is adjusted.

The idea to reduce the number of photons, that hit the PHD even more, is to place the first diaphragm at the beginning of the tube. A significant part of the incoming photons is instantly scattered back at the first diaphragm and has no chance to be reflected at the tube, to get beyond the first diaphragm. When the first diaphragm is positioned at 50 mm, as in the simulation before, much more photons can be reflected and thus pass the diaphragm system. To substantiate this theory, another 100 simulation of  $1 \cdot 10^5$  events each are performed. The diaphragms are positioned at 1 mm, 100 mm and 150 mm. The results show, that the number of photons that hit the PHD is lower than before. The mean value of hitting events is  $n_{hit,mean} = 66.8$  and the statistical error is  $\Delta n_{hit,mean} = 0.86$ . The sum for the 100 simulations and the error are:

$$n_{hit,sum} = 6675 \quad , \quad \Delta n_{hit,sum} = \sqrt{n_{hit,sum}} = 81.7 \quad (9.5)$$

The reduction factor for the simulation with the diaphragms at positions 1, 100 and 150 mm relative to the simulation without diaphragms is:

$$r = \frac{6675}{146715} = 0.0455 \quad (9.6)$$

With the result of the different simulations, the design of the tubes is determined as follows: the full length is set to 200 mm and the diaphragm length to 5 mm. Three diaphragms are used and their configuration is similar to the last simulation.

### 9.1.2 Measurements with the improved tube

The tubes were built with a full length of 200 mm and an inner diameter of 26 mm. One diaphragm is fixed in the middle of the tube, the other two diaphragms can be screwed from both



sides into the tube and so be adapted seamlessly to any position. Figure 9.6 shows photos of the tube and the PHD. The top picture shows a side view of the tube and the PHD, the bottom left picture shows a front view of the PHD and the bottom right picture shows a front view of the tube. The diaphragms, included in the tube, can be seen. To check if the tubes are identical



Figure 9.6: Photos of the tube and the PHD. Top: side view of the tube and the PHD, bottom left: front view of the PHD, bottom right: front view of the tube.

in their impacts on the measurement, a light field is scanned with both tubes under the same conditions. Figure 9.7 shows the measured data of the two tubes. The first diaphragm is adjusted at the front position of the tube, at 0 mm, the second diaphragm is fixed at the center, at 100 mm and the third diaphragm is adjusted at 150 mm. As the simulations show, this configuration should block most of the reflected photons. The measuring points of both tubes do not differ much. The differences between both measurements are of the order of  $0.2 \cdot 10^{-12}$ . The relative differences are of the order of 0.1 – 0.2 %. Hereinafter both tubes are treated as equal. To check, if the measured light field is not significantly disturbed by reflected light any more, data of another measured light field is fitted with a  $a/x^2$  function. The top picture in figure 9.8 shows the fitted light field over the whole range. There are some systematic differences between the fit function and the data between 2400 and 2600 mm, but at greater distances the data fits very well to the function. These differences can be systematic effects that are not yet understood, or maybe its just a drift of the pico amperemeter, that can be decisive at low currents. As the



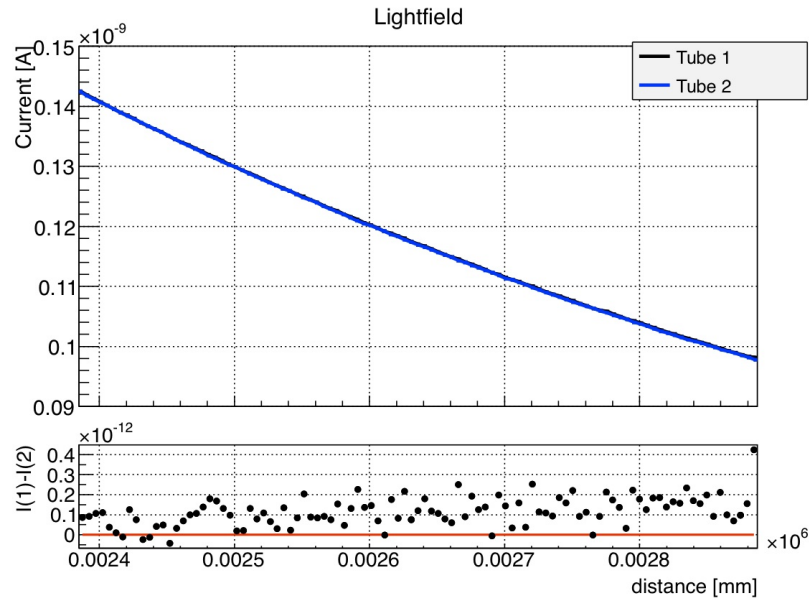


Figure 9.7: Light field measurement of the two tubes with the first diaphragm at 0 mm, the second diaphragm at 100 mm and the third diaphragm at 150 mm.

extrapolation is made for higher distances, the differences at lower distances should not matter very much. If the fit starts at 2600 mm, the fit quality is much better. The residuals seem to be deviated statistically around zero between 2600 and 2900 mm. The value of the residuals is again of the order of  $1 \cdot 10^{-13}$  A, but the absolute values of the light field are much higher as for the light field measurement in section 7.6. That is another confirmation, that the residuals mainly result from the drift of the picoamperemeter.

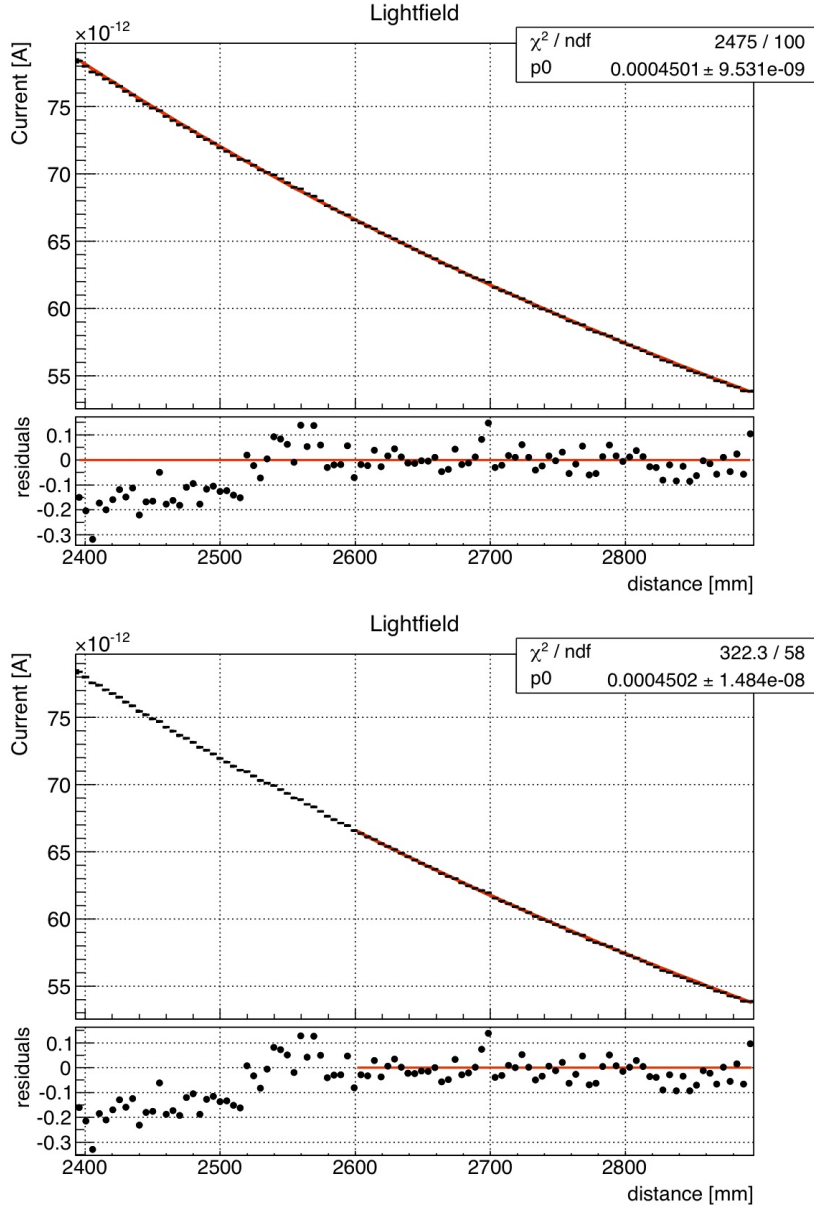


Figure 9.8: Top: measured light field and a  $a/x^2$  fit over the whole range, bottom: fit starting at a distance of 2600 mm.

## 9.2 Calibration of the diaphragm

A new calibration of the diaphragm with a diameter of  $\approx 1.3$  mm is made by scanning a light field with a new tube in front of the PHD and with and without the diaphragm. Both light fields have a  $1/x^2$  shape as shown in figure 9.9. The measured light field with the diaphragm is scaled up by a factor of 45 to see both shapes. The ratio  $A_{0,2}$  is calculated for every distance in the light field and the mean value and its error are calculated:

$$A_{0,2} = \frac{I_{\text{no diaphragm}}}{I_{\text{diaphragm 2}}} = 45.4666 \pm 0.0013 \quad (9.7)$$

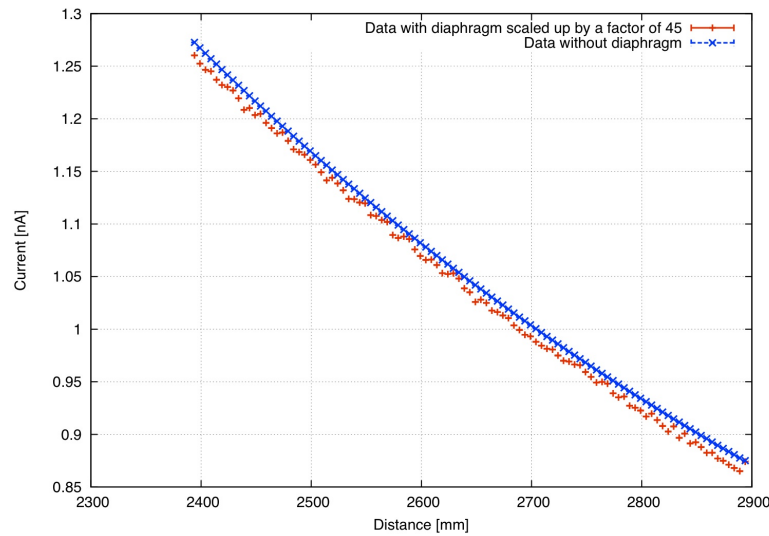


Figure 9.9: Light field scan for the calibration of the diaphragm.

### 9.3 Design of the improved test bench

The provisional test bench was very susceptible to disorders. The problem of the reflected light as discussed in detail is removed by the new tube design, but also mechanical effects can distort the measurement results. Switching the measured PMT causes displacements of the unfixed cardboard box or of the scanner. So it is necessary to adjust the right position of any involved element before each measurement. This takes a lot of time and is not always very exact, thus, it is hardly possible to repeat measurements under the same conditions. The idea to improve the test bench design is, thus, to make it more stable and remove some known systematic effects like the problem with the reflected light.

The design of the new test bench is described in the following paragraph. The box surrounding the PMT is made of plywood and is fixed on the table, that is responsible for the rotational scans. It consists of four wall parts and a cap, arranged with overlaps to block the light. One tube can be put in the front end of the box pointing towards the light source and its position can be adjusted vertically. In addition, a variable extension can be mounted on the end of the tube, to be able to adapt the rotational radius of the scans to the radius of curvature of the PMT, to guarantee perpendicular incidence of light at the PMT front window. The light field scanner is directly fixed at the same table as the box. Figure 9.10 shows photos of the test bench with the black box and the mounted scanner. This overall fixed configuration provides mechanical stability and thus stability of the measurement results. The second tube is mounted on the scanner in front of the PHD. As shown in subsection 9.1.2, both tubes, the one mounted in front of the PMT, the other one mounted in front of the PHD, perform the same shielding of reflected light and thus the measurement conditions for the light field scan and the waveform measurements are the same.

Figure 9.11 shows photos of the inside of the black box. The scanning device for the rotational scans and the possibility to extend the tube is shown. A new Hamamatsu R12199-02 PMT is

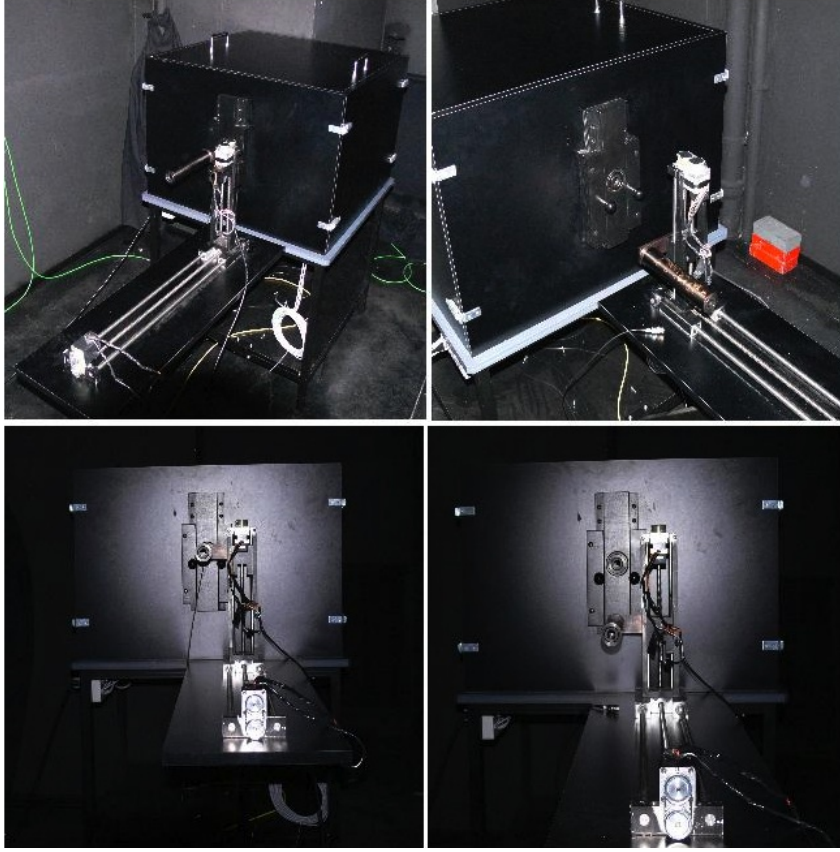


Figure 9.10: Photos of the test bench. Top left: the black box with mounted scanner in front, the tube with the PHD is in the position for the light field measurement. Top right: the black box and the scanner driven down for the waveform measurement with the PMT. Bottom left: front view of the black box and the scanner at light field measurement position. Bottom right: front view at driven down position of the scanner.

shown at different rotation angles. If the radius of curvature of the PMT front window is equal to the radius of rotation, perpendicular incidence of light at the photocathode is guaranteed.

## 9.4 Error calculation

Some more sources of errors are investigated for the new test bench. To illustrate that, the equation to calculate the detection efficiency with the single measurement parameters is shown again:

$$DE = \frac{N_{pe}}{N_{ph}} = \frac{N_{pe} \cdot QE_{PHD} \cdot f \cdot e \cdot A}{I_{PHD}}, \quad (9.8)$$

where  $N_{pe}$  is the number of measured photoelectrons per pulse,  $N_{ph}$  is the number of photons per pulse,  $QE_{PHD}$  is the quantum efficiency of the photodiode at the wavelength of the LED,  $f$  is the frequency of the light pulses,  $A$  is the diaphragm calibration factor and  $I_{PHD}$  is the current at the position of the diaphragm, extrapolated from the light field. The gaussian error propagation with the known statistical errors is:

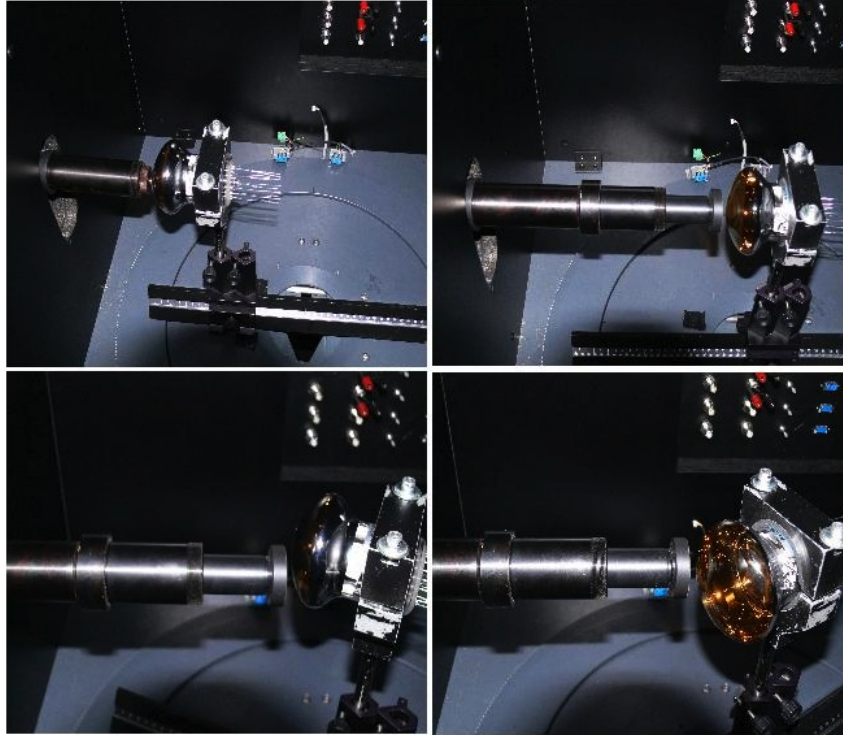


Figure 9.11: Photos of the inside of the test bench. Top left: the tube and the mounted PMT with an angle of  $0^\circ$ . Top right: tube extension to adjust the radius of rotation to the radius of curvature of the PMT front window. Bottom left: PMT rotated in one direction. Bottom right: PMT rotated in the other direction.

$$\Delta DE = DE \cdot \sqrt{\left(\frac{N_{pe}}{\Delta N_{pe}}\right)^2 + \left(\frac{f}{\Delta f}\right)^2 + \left(\frac{A}{\Delta A}\right)^2 + \left(\frac{I_{PHD}}{\Delta I_{PHD}}\right)^2} \quad (9.9)$$

The statistical error of the measured number of photoelectrons per pulse  $\Delta N_{pe}$  is known from the gauss fit of the histogram of charge or is a  $\sqrt{n}$  error if the number of photoelectrons is extracted from the histogram of charge with the threshold method, described in section 7.1. This error is individual for every histogram of charge and so for every waveform measurement with the PMT.

The statistical error of the current at the position of the diaphragm  $\Delta I_{PHD}$  is extrapolated from the light field and so is calculated via the errors of the fit variables. In the case of a  $I(x) = a/x^2$  fit the error is:

$$\Delta I(x_{\text{dist diaphragm}}) = \frac{1}{x_{\text{dist diaphragm}}^2} \cdot \Delta a = \Delta I_{PHD} \quad (9.10)$$

The statistical error of the diaphragm calibration factor  $\Delta A$  is calculated in section 9.2. This value is fixed if the diaphragm with a radius of  $\approx 1.3$  mm is used for the measurement. The calibration factor is:

$$A_{0,2} = \frac{I_{\text{no diaphragm}}}{I_{\text{diaphragm 2 mm}}} = 45.4666 \pm 0.0013 \quad (9.11)$$

The statistical error of the frequency  $\Delta f$  is calculated by measuring the current with the PHD while it is illuminated with the light source. The frequency output at the signal generator is

switched between  $f_{PMT} = 0.1$  MHz, the frequency with which the PMT waveforms are measured and 5 MHz, the maximum frequency which is adjusted during the light field measurement. The ratio of the measured currents gives the real frequency, that is used to calculate the detection efficiency. A calibration measurement gives a value of the true frequency of more than 5 MHz, the statistical error is calculated with the errors of the current measurement. The true value of the frequency  $f_{true}$  is:

$$f_{true} = \frac{I_{f=5MHz}}{I_{f=0.1MHz}} \cdot 0.1MHz = (5.245 \pm 0.002)MHz \quad (9.12)$$

## 9.5 Measurements with the improved test bench

The result of the measurement of the detection efficiency and the quantum efficiency of ten Hamamatsu R12199-02 PMTs and the calculation of the collection efficiency are presented in this section. The detection efficiency is measured with the improved test bench. The quantum efficiency is, in this case, also measured with a LED that has nearly the same spectrum as the LED used for the detection efficiency measurement. Table 9.1 shows the measured values of the quantum efficiency, detection efficiency and the calculated collection efficiency for seven of the ten measured PMTs. The fit of the remaining three PMTs is not good with a  $\chi^2$  of more than 2, so the values are not shown. The values of the detection efficiency and the quantum efficiency were measured at the center position of the photocathode. The errors of the detection efficiency are calculated as shown in section 9.4. The errors of the quantum efficiency and the collection efficiency are calculated with an error propagation as well. Figure 9.12 shows a fit of

Serial number	$QE$	$\Delta_{stat}QE$	$DE$	$\Delta_{stat}DE$	$CE$	$\Delta_{stat}CE$
6108	0.2089	0.0038	0.1741	0.0010	0.834	0.016
6123	0.1856	0.0033	0.1649	0.0053	0.888	0.033
6155	0.2061	0.0037	0.1951	0.0025	0.946	0.021
6161	0.2121	0.0038	0.1888	0.0019	0.890	0.018
6165	0.2273	0.0041	0.1972	0.0018	0.868	0.017
6167	0.2262	0.0041	0.1995	0.0010	0.882	0.016
6171	0.2191	0.0039	0.1949	0.0008	0.890	0.016

Table 9.1: Values of the quantum efficiency, detection efficiency and collection efficiency of seven Hamamatsu R12199-02 PMTs and its errors.

one measured histogram of charge. The number of photoelectrons per pulse is relatively high. The overlap of the gaussian fit of the pedestal peak and the gaussian fit of the single electron peak is relatively high and the number of photoelectrons per pulse, calculated with the threshold method differs from the number calculated with the fit values. The values extracted from the fit are shown in table 9.1. The detection efficiency of the different PMTs was measured with always the same high voltage of 1200 V. Therefore, the gain, and so the amount of photon events, that can not be distinguished from the pedestal can differ. To do a better characterization, it is necessary to measure the detection efficiency with a high voltage, where each PMT has a characteristic gain of  $5 \cdot 10^6$ , as it will be during the continuous operation of the detector.



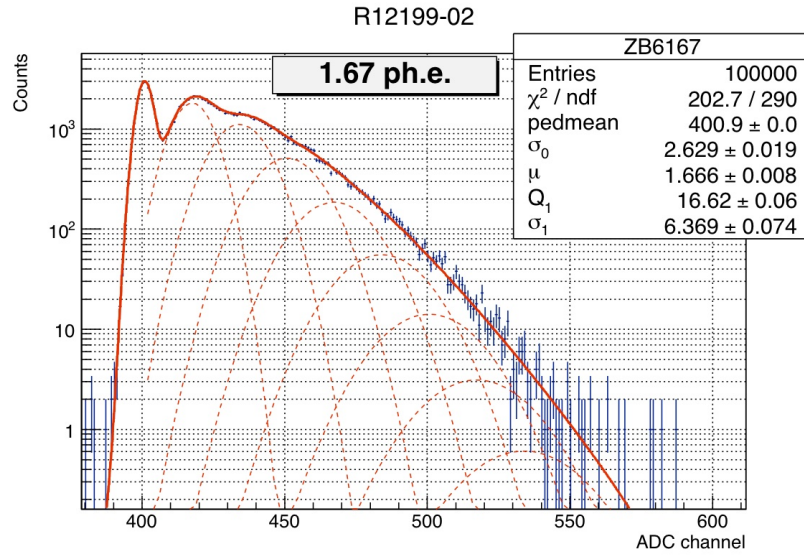


Figure 9.12: One measured histogram of charge.

## 9.6 Linear Scan

This section shows the results of a linear scan of one PMT, also measured in section 9.5 (serial number 6171). A linear scan was made as shown in figure 8.2. The photocathode sensitivity was measured as the quantum efficiency and the anode sensitivity was measured in pulse mode as the detection efficiency for different positions on the photocathode, but without a reference measurement with the PHD. The absolute quantum efficiency and detection efficiency values shown in table 9.1 are used to calculate the quantum efficiency and detection efficiency for the different positions on the photocathode. As the QE and DE scans were made under the same conditions concerning the position and angle of incidence on the photocathode, the collection efficiency can be calculated for the different positions on the photocathode. The values of the quantum efficiency, the detection efficiency and the collection efficiency for the different positions on the photocathode are shown in figure 9.13. It can be seen that the detection efficiency and the quantum efficiency increase slightly from the center position towards the edges. This can be explained by the photons starting to hit the reflecting area shown in figure 8.2. As described in section 8.2, photons hitting the reflecting area can produce photo electrons there or they can be scattered to the photocathode to produce a photo electron. According to the fact that the angle of incidence differs more and more from  $90^\circ$  for greater distances from the center, the detection efficiency starts to decrease at a position of roughly 25 – 30 mm. The quantum efficiency does not start to decrease until roughly 35 mm distance from the center. The reason for that is, that the produced photo electrons at the reflecting areas are measured with a higher probability at the quantum efficiency measurement than at the detection efficiency measurement (see section 8.2). This effect is also the main reason for the decrease of the collection efficiency towards the edges of the photocathode.

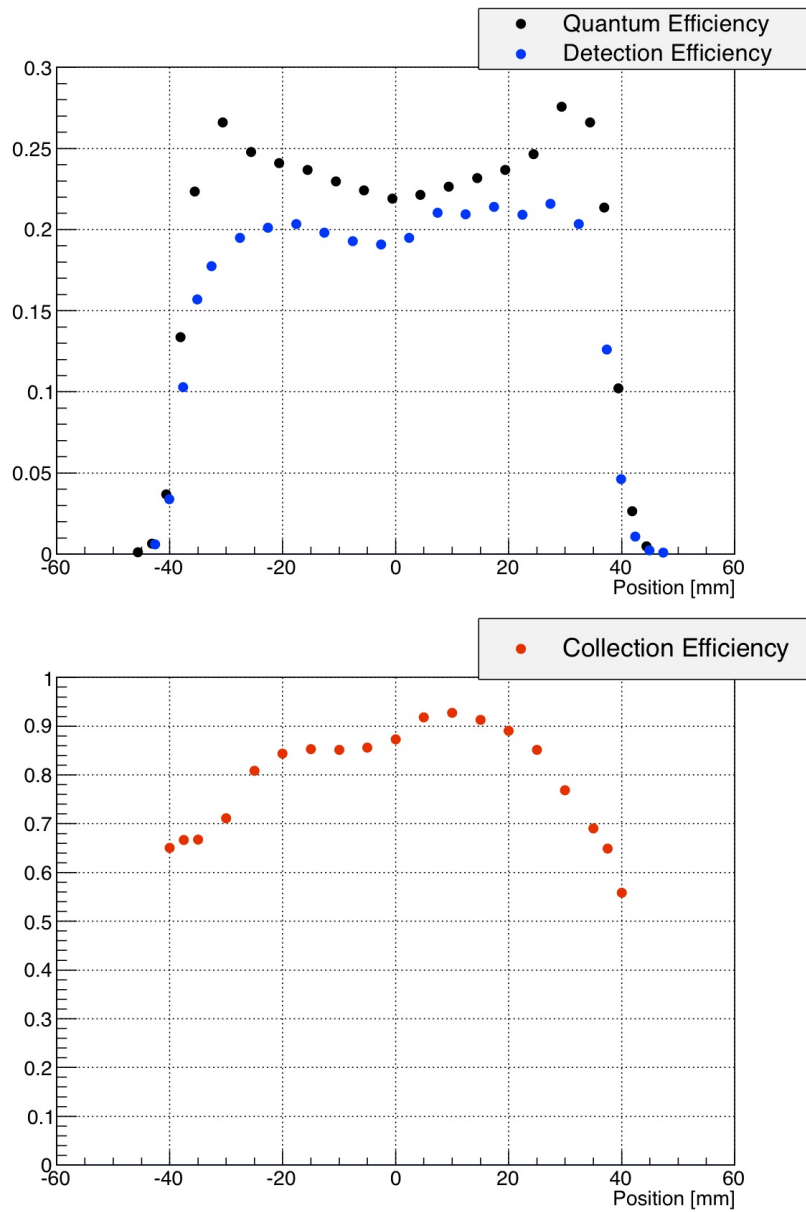


Figure 9.13: Linear scan of the quantum efficiency and the detection efficiency (top) and the calculated collection efficiency (bottom).



# Chapter 10

## Summary and Outlook

The detection efficiency, measured in pulse mode, is an important selection criterion for a PMT to be used in the KM3NeT project. The aim of this thesis was to determine this parameter. Therefore, a test bench was designed and installed at the ECAP. Removing systematic error sources, like for instance the problem of the reflected light, represents another essential part of the work. The amount of reflected light, that distort the measurement results was reduced by the development of a protective tube, described in section 9.1. The quantum efficiency was measured to calculate the collection efficiency. The peak wavelength of the used light source is similar to the characteristic wavelength 470 nm (see figure 7.3). This wavelength is the maximum of the multiplication of an expected Cherenkov spectrum with the spectral transparency of water and so of the expected spectrum at an optical module. The mean value of the quantum efficiency of the seven measured Hamamatsu R12199-02 PMTs is 21.22 %. This value exceeds 20 % and so fulfils the selection criterion. Only one single value of the measured quantum efficiency is below 20 % (see table 9.1). The mean value of the detection efficiency is 18.78 % and the mean value of the collection efficiency is 88.7 %. This value is slightly smaller than 90 % of collection efficiency, which current PMTs are claimed to exceed.

The existing differences between the collection efficiency, a PMT has under realistic conditions and the ideal collection efficiency a PMT has, have to be investigated in the future. In continuous operation, the high voltage of the PMTs will be adjusted, that they have a gain of  $5 \cdot 10^6$ . In this case, the charge produced by a photon can be too low to distinguish it from a pedestal event. Therefore, the collection efficiency is smaller as for ideal conditions, where the gain is high enough to distinguish nearly all photon events from the pedestal.

As prototypes of optical modules for the KM3NeT project are planned to be constructed at the ECAP, the design of the detection efficiency test bench was adjusted to allow for a detection efficiency measurement of an optical module. It is also planned to calculate the effective area of a PMT or of an optical module with the informations gained from a detection efficiency measurement.



# List of Figures

2.1	Energy spectrum of cosmic rays . . . . .	10
2.2	Sources of cosmic rays . . . . .	11
3.1	Cosmogenic neutrino flux . . . . .	15
3.2	High energy neutrino-nucleon cross section . . . . .	16
3.3	Glashow resonance of neutrino-electron interaction . . . . .	16
4.1	Cherenkov cone and spherical Cherenkov front . . . . .	18
4.2	Relative transparency of water and Cherenkov spectrum . . . . .	20
4.3	Schematic picture of the ANTARES detector . . . . .	20
4.4	Possible sites of the KM3NeT detector . . . . .	21
4.5	Artist view of the KM3NeT detector . . . . .	22
4.6	The KM3NeT DOM and string . . . . .	23
5.1	Schematic picture of a PMT . . . . .	25
5.2	Spectral quantum efficiency of a ETEL PMT . . . . .	27
5.3	Histogram of charge with a single electron spectrum . . . . .	29
6.1	Photo of an ETEL D783KFLA PMT . . . . .	32
6.2	Photo of a Hamamatsu R12199-02 PMT . . . . .	32
7.1	Histogram of charge and threshold . . . . .	34
7.2	Quantum efficiency of the calibrated photodiode . . . . .	35
7.3	Spectrum of a LED . . . . .	35
7.4	Measurement procedure . . . . .	36
7.5	Photo of the light source . . . . .	37
7.6	Light field with much reflections . . . . .	38
7.7	Light field with mounted tube and covered table . . . . .	38
7.8	Light field with a $a/x^b$ fit . . . . .	39
7.9	Calibration of the diaphragms . . . . .	40
7.10	Multi view on the integration of the waveforms . . . . .	41
7.11	Fit of the histogram of charge . . . . .	43
7.12	Histogram of charge and threshold method . . . . .	44
7.13	Detection efficiency scan of the ETEL D783KFLA PMT . . . . .	44
7.14	Light field with covered tube . . . . .	46
7.15	Histogram of charge with broad pedestal . . . . .	47
7.16	Modified histogram of charge . . . . .	47

7.17	Detection efficiency scan of the Hamamatsu R12199 PMT . . . . .	48
8.1	Normalized spectrum of the Xenon light bulb . . . . .	50
8.2	Emphasis of the principle of the scans . . . . .	51
8.3	Quantum efficiency and detection efficiency scan of the ETEL D783KFLA PMT	52
8.4	Quantum efficiency and detection efficiency scan of the Hamamatsu R12199 PMT	53
9.1	Sketch of the tube layout . . . . .	55
9.2	Tube simulation with different absorption coefficients . . . . .	56
9.3	Tube simulation with only hitting events . . . . .	57
9.4	Distribution of the single simulations . . . . .	58
9.5	Tube simulation with diaphragms . . . . .	59
9.6	Photos of the tube and the PHD . . . . .	60
9.7	Light field measurement with the new tubes with diaphragms . . . . .	61
9.8	Light field and $a/x^2$ fit with the new tube . . . . .	62
9.9	Light field and the calibration of the diaphragm . . . . .	63
9.10	Photos of the outside of the test bench . . . . .	64
9.11	Photos of the inside of the test bench . . . . .	65
9.12	Histogram of charge of one of the ten measured Hamamatsu R12199-02 PMTs	67
9.13	Linear QE and DE scan . . . . .	68

# List of Tables

4.1	Absorption and scattering length of light in water . . . . .	18
4.2	Transmission coefficient of water and relative number of Cherenkov photons . .	19
7.1	Detection efficiency of the ETEL D783KFLA PMT . . . . .	45
7.2	Detection efficiency of the Hamamatsu R12199 PMT . . . . .	48
9.1	Quantum efficiency, detection efficiency and collection efficiency of seven Hamamatsu R12199-02 PMTs . . . . .	66



# Bibliography

- [1] Ulrich F. Katz and Christian Spiering. High-Energy Neutrino Astrophysics: Status and Perspectives. *Prog.Part.Nucl.Phys.*, 67:651–704, 2012.
- [2] C. Grupen. *Astroparticle physics*. Springer-Verlag Berlin Heidelberg, 2005.
- [3] K. Kotera, D. Allard, and A.V. Olinto. Cosmogenic Neutrinos: parameter space and detectability from PeV to ZeV. *JCAP*, 1010:013, 2010.
- [4] Amy Connolly, Robert S. Thorne, and David Waters. Calculation of High Energy Neutrino-Nucleon Cross Sections and Uncertainties Using the MSTW Parton Distribution Functions and Implications for Future Experiments. *Phys.Rev.*, D83:113009, 2011.
- [5] Amanda Cooper-Sarkar, Philipp Mertsch, and Subir Sarkar. The high energy neutrino cross-section in the Standard Model and its uncertainty. *JHEP*, 1108:042, 2011.
- [6] The KM3NeT Consortium. Detector Simulations for KM3NeT, Work Package D, V2.3, 2011. Internal note available online at <http://www.km3net.org/internal.php>; visited on June 25th 2012.
- [7] ANTARES Collaboration. ANTARES homepage. Available from <http://antares.in2p3.fr>; visited on August 10th 2012.
- [8] P. Bagley et al. (The KM3NeT Consortium). Technical Design Report, 2011. Available online at <http://www.km3net.org>; visited on October 11th 2012.
- [9] The KM3NeT Consortium. KM3NeT homepage. Available from <http://www.km3net.org/home.php>; visited on October 11th 2012.
- [10] Hamamatsu Photonics. *Photomultiplier Tubes - Basics and Applications*, 3rd edition, 2006. Available from [http://sales.hamamatsu.com/assets/applications/ETD/pmt\\_handbook\\_complete.pdf](http://sales.hamamatsu.com/assets/applications/ETD/pmt_handbook_complete.pdf); visited on November 8th 2012.
- [11] S-O Flyckt and Carole Marmonier. *Photomultiplier Tubes - Principles and Applications*, 2002. Available from [www.pv.infn.it/~debari/doc/Flyckt\\_Marmonier.pdf](http://www.pv.infn.it/~debari/doc/Flyckt_Marmonier.pdf); visited on November 8th 2012.
- [12] E.H. Bellamy, G. Bellettini, F. Gervelli, M. Incagli, D. Lucchesi, et al. Absolute calibration and monitoring of a spectrometric channel using a photomultiplier. *Nucl.Instrum.Meth.*, A339:468–476, 1994.





# Danksagung

Ich danke in erster Linie meiner Familie, die mich während dem gesamten Studium aber auch gerade während meiner Masterarbeit sowohl mental als auch finanziell unterstützt haben.

Außerdem gilt mein Dank Uli Katz und Oleg Kalekin, die diese Masterarbeit ermöglicht, betreut und unterstützt haben. Alle Fragen und Probleme die im verlauf der Arbeit auftauchten wurden von ihnen mit Geduld und Sachverstand beantwortet und gelöst.

Außerdem bedanke ich mich bei meinen Zimmergenossen Dominik und Lew für den scheinbar uferlos mächtigen Umfang an Hilfe den sie mir geleistet haben.

Außerdem seien herzlichst bedankt: Korrekturleser, Werkstattmitarbeiter, Admins und Gisela Anton als Zweitgutachter.



# Erklärung

Hiermit bestätige ich, dass ich diese Arbeit selbstständig und nur unter Verwendung der angegebenen Hilfsmittel angefertigt habe.

Erlangen, 15.11.2012

Jonas Reubelt